# Regional modeling of internal tide dynamics around New Caledonia. Part I: Coherent internal tide characteristics and sea surface height signature

Arne Bendinger[1], Sophie Cravatte[1], Lionel Gourdeau[1], Laurent Brodeau[2,a], Aurélie Albert[2], Michel Tchilibou[1,b], Florent Lyard[1], and Clément Vic[3]

[1]Université de Toulouse, LEGOS (CNES/CNRS/IRD/UPS), Toulouse, France
[2]Université Grenoble Alpes, CNRS, INRAE, IRD, Grenoble INP, Institut des Géosciences de l'Environnement, Grenoble, France
[3]Laboratoire d'Océanographie Physique et Spatiale, Univ. Brest, CNRS, Ifremer, IRD, Plouzané, France
[a]now at: DATLAS, Grenoble, France
[b]now at: CLS, Ramonville Saint-Agne, France

**Correspondence:** Arne Bendinger (arne.bendinger@univ-tlse3.fr)

**Abstract.** The Southwestern Tropical Pacific exhibits a complex bathymetry and represents a hot spot of internal tide generation. Based on a tailored high-resolution regional model, we investigate for the first time the internal tide field around the New Caledonia islands through energy budgets that quantify the coherent internal tide generation, propagation, and dissipation. A total of 15.27 GW is converted from the barotropic to the baroclinic M2 tide with the main conversion sites associated with the most prominent bathymetric structures such as continental slopes and narrow passages in the north (2.17 GW) and ridges and seamounts south of New Caledonia (3.92 GW). The bulk of baroclinic energy is generated in shallow waters around 500 m depth and on critical to supercritical slopes highlighting the limitations of linear semi-analytical models in those areas. Despite the strongly dominant mode-1 generation, more than 50 % of the locally generated energy either dissipates in the near-field close to the generation sites or loses coherence. The remaining baroclinic energy propagates within well-defined tidal beams with baroclinic energy fluxes of up to 30 kW m$^{-1}$ toward the open ocean. The New Caledonia site represents a challenge for SWOT (Surface Water Ocean Topography) observability of balanced motion in the presence of internal tides with sea surface height (SSH) signatures of > 6 cm at similar wavelengths. We show for our study region that a correction of SSH for the coherent internal tide potentially increases the observability of balanced motion from > 160 km to well below 100 km.

## 1 Introduction

The flow of barotropic tidal oceanic currents over bathymetry such as continental slopes, ridges, and seamounts represent a major source for baroclinic energy in the global ocean in form of internal tides (i.e. internal waves at tidal frequency) expressed by high-frequency fluctuations and vertical displacements of isopycnal surfaces (Bell Jr, 1975; Smith and Young, 2002; Garrett and Kunze, 2007). From a global point of view, internal tides have received increasing attention in recent decades as they provide a route to energy dissipation away from lateral boundaries and the surface through diapycnal mixing with important

20 implications for open ocean mixing and the global oceanic energy budget (e.g. Munk and Wunsch, 1998; Melet et al., 2013; Waterhouse et al., 2014; Kunze, 2017a, b).

Internal tides express themselves in vertical oscillations of density surfaces with strong baroclinic velocities. They are characterized by a complex vertical structure that can be described by a discrete set of vertical normal modes via the Sturm-Liouville problem (Gill, 1982; Arbic et al., 2018; Buijsman et al., 2020). Low-vertical modes have large horizontal wavelengths

25 ($\mathcal{O}$(150 km)), usually form over large-scale topographic features, and propagate over large distances ($\mathcal{O}$(1000 km)); Dushaw et al., 1995; St. Laurent and Garrett, 2002; Alford, 2003; Zhao et al., 2010, 2016). In contrast, high-vertical modes feature smaller horizontal wavelengths that are generated over smaller-scale topographic features. They tend to dissipate locally not far away from the formation sites due to their lower group velocities and higher vertical shear (Zhao et al., 2016; Vic et al., 2019). Characterizing internal tides, their vertical structure and propagation is thus key to better understand their contribution

30 to mixing.

Yet, it is still challenging, both through observations or model experiments. Some scattered in-situ observations with high-frequency sampling, such as moorings, can help to characterize these processes at some locations (e.g., Zilberman et al., 2011; Vic et al., 2018) but they do not provide a global view. Alternatively, altimetric Sea Surface Height (SSH) observations have been extensively used to estimate globally the SSH imprint of internal tides by using e.g. empirical models that are based on an

35 up to 20-year long record of conventional altimeter missions (Zhao et al., 2016; Ray and Zaron, 2016; Zaron, 2019; Ubelmann et al., 2022). These estimates have provided us with a robust representation of the coherent internal tide which is defined here as the phase-locked internal tide being constant in amplitude and phase, and determined over a long time series. However, satellite altimetry provides in general very limited information about the internal tides' vertical structure, allowing the detection of the first and second vertical modes only.

40 The characterization of internal tides with its vertical modes (each associated with a different wavelength) and its signature in SSH is an important task for the SWOT Water Ocean Topography (SWOT) satellite mission (launched in December 2022). SWOT is expected to provide new insights into small-scale ocean dynamics resolving wavelengths by up to ten times higher resolution (down to 15 km; Fu et al., 2012; Fu and Ubelmann, 2014) than conventional altimetry ($\mathcal{O}$ 100 km; Ballarotta et al., 2019) with SSH imprints from meso- and submesoscale dynamics down to high-frequency internal wave motion, and the inter-

45 action between each other (?Morrow et al., 2019)(Fu and Ferrari, 2008; Morrow et al., 2019). From an oceanographic point of view, the characterization of the meso- and submesoscale circulation is the primary objective of SWOT (Morrow et al., 2019). The challenge lies in disentangling the measured SSH signal associated with balanced and unbalanced motions, i.e. eddies and gravity waves, since they can feature similar spatial scales. This highlights the need of a detailed picture of internal tide dynamics to properly derive meso- and submesoscale motions (Zaron, 2019; Carrere et al., 2021). Numerical modeling has

50 been playing an important role in partly overcoming the constraints of in-situ observations and altimetry. Dedicated studies of internal tide characteristics and energetics near internal tide generation hot spots have been conducted in various regions such as the Hawaiian Ridge (Carter et al., 2008), Luzon Strait (Kerry et al., 2013), Solomon Sea (Tchilibou et al., 2020), Amazonian Shelf (Tchilibou et al., 2022), and the Mid-Atlantic Ridge (?)(Lahaye et al., 2020). The energy converted from barotropic to baroclinic tides, the distribution of the vertical modes generated, the local ratio between dissipation and conversion, and the

energy propagation are all heavily depending on the local bathymetric features and the background state emphasizing the need for regional focus with high-resolution regional simulations.

Here, we provide the first comprehensive description of the internal tide field around New Caledonia in the Southwestern Tropical Pacific using the output of a tailored high-resolution regional simulation from a full-model calendar year (Fig. 1). This region has not received much attention despite being known as an internal tide generation hot spot from numerical modeling of internal tides in its early stages (Niwa and Hibiya, 2001). It is characterized by complex bathymetry of large-scale ridges, very steep slopes, shelf breaks, basins, and seamounts at mid-depths and near-surface that give rise to propagating tidal beams over several hundreds of km and significant signatures in SSH as deduced from satellite altimetry (Ray and Zaron, 2016). New Caledonia also represents an interesting site to study eddy-internal tide interactions due to a complex regional circulation (Qu and Lindstrom, 2002; Kessler and Cravatte, 2013; Cravatte et al., 2015). Through the interaction with the background currents, the internal tide field around New Caledonia is potentially subject to temporal variability, also referred to as tidal incoherence in literature (e.g. Dunphy and Lamb, 2014; Dunphy et al., 2017; Ponte et al., 2017; Lamb and Dunphy, 2018; Shakespeare and Hogg, 2019). An additional reason to study the internal tide around New Caledonia is their potential role on the marine biodiversity for which the region is internationally recognized (Payri et al., 2019). This is especially true south of New Caledonia where seamounts and ridges are hots spots of biodiversity providing marine habitats for marine mammals, fish, and small-scale organisms (Payri and de Forges, 2006; Ganachaud et al., 2010; Gardes et al., 2014; Menkès et al., 2015). Internal tides may also have important implications for coastal ecosystems, mitigating heat stress (Wyatt et al., 2020, 2023), or enhancing upwelling of nutrient-rich waters to the surface (Wolanski and Pickard, 1985; Leichter et al., 2003).

Lastly, the region is crossed by the SWOT swaths during SWOT's fast-sampling phase (1-day repeat orbit, Fig. 1a). In this context, New Caledonia serves as a calibration and validation (CalVal) site within the SWOT program and the associated Adopt-A-Crossover (AdAC) consortium. A dedicated field campaign has been carried out in spring 2023 to collect high-frequency measurements of the governing fine-scale physics. It thus represents a unique opportunity to address SSH observability of meso- and submesoscale dynamics, internal tides, and their interaction.

Due to the study's extent, this work is subject to a series of two papers. Part I focuses on stationary, coherent internal tides whereas Part II focuses on non-stationary, incoherent internal tides addressing mesoscale activity as a source of this incoherence.

This study's overall objective for Part I is twofold. 1) A detailed introduction to the regional modeling effort that has been explicitly designed to shed light on the internal tide dynamics around New Caledonia in the framework of SWOT-AdAC, including a model assessment 2) A detailed description of the coherent internal tide energetics providing a first picture of the local dynamics at work. Here, we will address the following scientific questions: What areas around New Caledonia are subject to internal tide generation and dissipation? What is the internal tide's modal content? How does the internal tide express in SSH, and at which wavelengths are we able to observe meso- and submesoscale processes?

The study is organized as follows. In Sect. 2, we introduce the high-resolution modeling strategy, the tidal analyses and diagnostics used in this study, as well as the different datasets or products used to assess our simulation. The model assessment is presented in Sect. 3, where we estimate the model ability to realistically simulate the mean circulation, the mesoscale activity,

90 and the barotropic tides. In Sect. 4, we quantify the energetics of the dominant internal tide, in the region around New Cale-
donia and in the hot spots of internal tide generation. Internal tide SSH signature is investigated in Sect. 5, in the context of
SWOT observability. We finish with a summary and discussion in Sect. 6.

## 2 Data and Methods

### 2.1 Model set-up

95 The model used in this study is based on the Nucleus for European Modeling of the Ocean (NEMO, code version 4.0.6, Madec
and Team) which solves the three-dimensional primitive equations on a staggered Arakawa-C type grid. The model grid con-
sists of a host grid (TROPICO12) at 1/12° horizontal resolution that spans the Pacific Ocean basin from 142° E - 290° E and
24° N - 46° S (Fig 1a). It features 125 vertical levels with 0.5 m thickness at the surface increasing toward 150 m in the deep
ocean with 75 vertical levels in the upper 1000 m (Fig 1b). In the vertical, the model uses a partial step z-coordinate with a
100 non-linear free surface.

Further, the model set-up features a horizontal grid refinement (nesting), named CALEDO60, at 1/60° horizontal resolution
(∼1.7 km grid-box spacing). In this particular region, it is expected to allow the model to be submesoscale-permitting. The
nesting grid is located in the Southwestern Tropical Pacific from 159.2° E - 172.4° E and 15.7° S - 28.8° S and encompasses
New Caledonia (see Fig. 1a). The nesting was set-up using an Adaptive Grid Refinement In Fortran (AGRIF, Debreu et al.,
105 2008), a tool explicitly designed for NEMO to set up regional simulations embedded in a pre-defined configuration. AGRIF
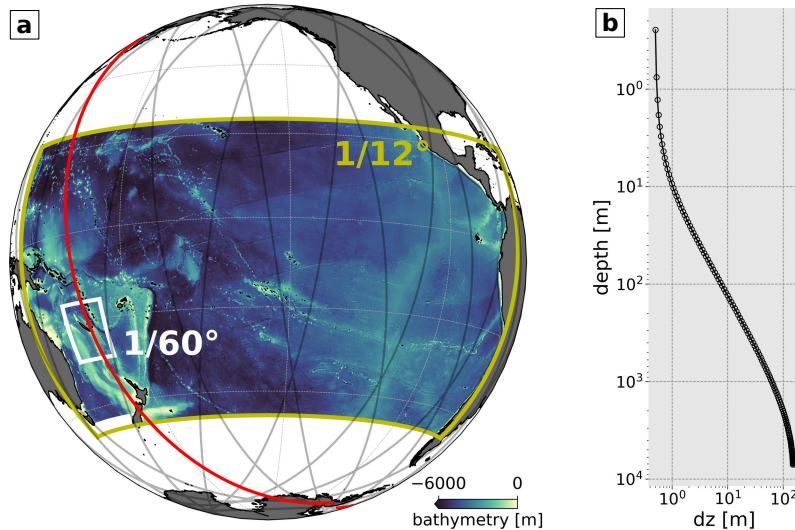
**Figure 1.** (a) Model set-up showing the host grid domain (TROPICO12, yellow box) and the nesting grid (CALEDO60, white box) including
the bathymetry (shading), and the SWOT CalVal orbit (black transparent lines) with the highlighted ground track (red line) that crosses the
CALEDO60 domain. (b) TROPICO12/CALEDO60 vertical resolution among 125 vertical levels.

enables the two-way lateral boundary coupling between the host and the nesting grid being integrated sequentially during the whole length of the simulation.

Laplacian isopycnal diffusion coefficients for tracers were chosen to be mesh-size dependent such that the tracer diffusion is scaled down from the host grid of 93 m$^2$ s$^{-1}$ to the nesting grid of 4 m$^2$ s$^{-1}$. Vertical eddy diffusivity is estimated by a TKE

110   turbulent closure scheme (Gaspar et al., 1990). It is based on a prognostic equation for turbulent kinetic energy and a closure assumption for turbulent length scales depending on vertical shear, stratification, vertical diffusion, and dissipation. The advection of momentum is parameterized by means of a third-order scheme based on upstream-biased parabolic interpolation (UBS).

Initial conditions for temperature and salinity for TROPICO12 and CALEDO60 are prescribed by the GLORYS2V4 oceanic

115   reanalysis (https://doi.org/10.48670/moi-00023). Atmospheric forcing is taken from ERA5 produced by the European Centre for Medium-Range Weather Forecasts (ECMWF, Hersbach et al., 2020) provided at hourly temporal resolution and a spatial resolution of 1/4°to compute surface fluxes using bulk formulae and the prognostic sea surface temperature from the model. Wind stress are computed following the methodology from Renault et al. (2016), i.e. wind speed minus surface currents. Both domains are forced by the tidal potential of the five major tidal constituents (M2, S2, N2, K1, O1). TROPICO12 is forced at its

120   open lateral boundaries with daily currents, temperature, and salinity, likewise using GLORYS2V4. In addition, TROPICO12 is forced at the open lateral boundaries by SSH and barotropic currents of the same five tidal constituents taken from the global tide atlas FES2014 (Finite Element Solution 2014, Lyard et al., 2021). We made this limited choice to allow the separation of these constituents at monthly timescales. Recent studies highlighted the importance of taking into account remote forcing of high-frequency oceanic variability for regional simulations, as it may represent a non-negligible source of energy

125   (?Nelson et al., 2020; Mazloff et al., 2020; Siyanbola et al., 2023)(Jeon et al., 2019; Nelson et al., 2020; Mazloff et al., 2020; Siyanbola et . Further, it was suggested that tidal accuracy and predictability increase when implementing a two-way nesting framework between the high-resolution regional domain and the lower-resolution host grid (?)(Jeon et al., 2019). The authors show that mass and energy are conserved with no evident discontinuities along the nesting boundaries.

Apart from increasing predictability through higher horizontal resolution of the nesting grid, it is argued that a realistic

130   bathymetry product is also essential. For the CALEDO60 domain, we used a specific bathymetric product based on the GEBCO_2019 grid (?)(GEBCO, 2019) and a compilation of multibeam echosounder data acquired over the years in the New Caledonia economic zone (Roger et al., 2021). The latter product, initially at 200 m resolution, only covers the area 155° E - 175.1° N, 14.1° S - 26.6° S. It has been combined with the GEBCO_2019 bathymetry product to cover the full domain.

Internal tides represent a large source of diapycnal mixing in the open ocean. The associated parameterization scheme devel-

135   oped by St. Laurent et al. (2002) is usually used in NEMO simulations. Here, it has been turned off because our simulation has a resolution large enough to resolve the internal wave dynamics. In fact, it has been recently suggested that turning off background components of the vertical mixing scheme improves the modeled kinetic energy levels (Thakur et al., 2022).

The bottom friction is parameterized using a logarithmic boundary layer with a drag coefficient of $3\times10^{-3}$ (maximum value of 0.1), a roughness of 2.5e-3$\times10^{-3}$ m, and a background kinetic energy of $1\times10^{-2}$ m$^2$ s$^{-2}$. These values yielded the best

140   visual agreement with respect to the mean regional circulation, i.e. the location and magnitude of zonal jets.

The model has been spun up for two years (model year 2012-2013) before being run for a total of five years (model year 2014-2018). Here, if not noted otherwise, we only focus on 2014 (neutral El Niño - Southern Oscillation conditions) with instantaneous fields saved hourly for the three-dimensional temperature, salinity, velocity, and surface fields (including SSH) for CALEDO60. For TROPICO12, the instantaneous three-dimensional variables are given at daily resolution, whereas the surface fields are saved at hourly resolution. A twin experiment with identical forcing and parameterization has been initialized, but without barotropic tide forcing. Being subject to a future study, here, it is only used to compare the energy spectrum with the tidal simulation.

## 2.2 Tidal analysis and diagnostics

### 2.2.1 Tidal harmonics

In order to investigate the tidal dynamics at play in the regional CALEDO60 simulation, we first apply a harmonic analysis on a full-model calendar year time series (model year 2014) of the three-dimensional velocity and pressure fields to extract the semidiurnal (M2, S2, N2) and diurnal (K1, O1) tidal constituents. The choice of a full-model calendar year relies upon a compromise between high computational expenses and the representative extraction of the coherent tide through a time series long enough to isolate seasonal and mesoscale variability. Therefore and if not noted otherwise, we define the coherent internal tide as the phase-locked internal tide with constant amplitude and phase referenced to the full-model calendar year time series.

### 2.2.2 Barotropic-baroclinic modal decomposition

The study of internal tides requires an accurate separation of the barotropic and baroclinic tides. The barotropic tide is directly linked to the astronomical tide forcing. In contrast to baroclinic tides, it is independent of depth and density stratification (Hendershott, 1981, cf Sect. 1). Several approaches to separate barotropic and baroclinic tides have been discussed in detail, for example in Kelly et al. (2010), Nugroho (2017), or in Tchilibou et al. (2020). Here, we use a vertical-mode decomposition approach by solving the Sturm-Liouville problem obeying a linear free-surface while assuming a flat bottom:

$$\frac{\partial^2 \Phi_n}{\partial z^2} + \frac{N^2}{c_n^2} \Phi_n = 0 \tag{1}$$

$$\Phi_n = \frac{c_n^2}{g} \frac{\partial \Phi_n}{\partial z} \quad \text{at} \quad z = 0, \quad \text{and} \tag{2}$$

$$\Phi_n = 0 \quad \text{at} \quad z = -H, \tag{3}$$

with the given buoyancy frequency $N$ defined as:

$$N^2 = -\frac{g}{\rho_0} \frac{\partial \rho}{\partial z}, \tag{4}$$

where $\rho$ is the potential density, $z$ the vertical depth vector, $g$ the gravitational acceleration, and $\rho_0$ the reference density. $c_n$ is the eigenspeed and $\Phi_n$ the eigenfunction describing the vertical structure for vertical velocity and displacement (McDougall

and Barker, 2011). It is related to the eigenfunction describing the vertical structure for horizontal velocity and pressure via:

$$\phi_n = \rho_0\, c_n^2\, \frac{\partial \Phi_n}{\partial z} \tag{5}$$

In practice, the Sturm-Liouville eigenvalue problem has been solved at each grid point of the model, using the annual mean density field referenced to the same period as the harmonic analysis above, for the ten lowest modes, where the lowest mode ($n = 0$) refers to the barotropic tide and $n \geq 1$ are the baroclinic modes. Based on the tidal harmonics determined in Sect. 2.2.1, the model ~~horizontal velocities and , vertical velocity , and pressure are then decomposed~~ variables are projected onto the orthogonal, ~~discretized~~ discrete set of normal vertical modes~~:~~, i.e.

$$[u(x,y,z,t),v(x,y,z,t),p(x,y,z,t)]= \sum_{n=0}^{9}[u_n(x,y,t),v_n(x,y,t),p_n(x,y,t)]\phi_n(z),$$

$$w(x,y,z,t)= \sum_{n=0}^{9}w_n(x,y,t)\Phi_n(z)$$

$$[\mathbf{u}(x,y,z,t),p(x,y,z,t)]= \sum_{n=0}^{9}[\mathbf{u}_n(x,y,t),p_n(x,y,t)]\phi_n(z), \tag{6}$$

for the horizontal velocity vector $\mathbf{u} = (u,v)$, pressure $p$, and

$$w(x,y,z,t) = \sum_{n=0}^{9}w_n(x,y,t)\Phi_n(z), \tag{7}$$

for the vertical velocity $w$, using a least squares fit method. If not specified otherwise, we define the baroclinic tide as the sum of modes 1-9. As will be seen in Sect. 4, this is sufficient in our study region, where low baroclinic modes are strongly dominant.

### 2.2.3 Energy equations

The redistribution and transfer of energy from the barotropic tide to the internal tide can be approximated by the barotropic and baroclinic energy equation neglecting the tendency term and nonlinear advection following Simmons et al. (2004), Carter et al. (2008), and Buijsman et al. (2014, 2017) since both terms were found to be at least one order of magnitude smaller:

$$\nabla_{\mathbf{h}} \cdot \mathbf{F_{bt}} + D_{bt} + C = 0, \tag{8}$$

$$\nabla_{\mathbf{h}} \cdot \mathbf{F_{bc}} + D_{bc} - C = 0, \tag{9}$$

where $\nabla_{\mathbf{h}} \cdot \mathbf{F}$ is the energy flux divergence with $\nabla_{\mathbf{h}} = (\partial/\partial x, \partial/\partial y)$ the horizontal gradient operator and $\mathbf{F} = (F_x, F_y)$ the energy flux vector, $D$ the energy dissipation, and $C$ the barotropic-to-baroclinic conversion term. The subscripts $_{bt}$ and $_{bc}$ stand

for the barotropic and baroclinic tide . In the barotropic energy equation, the conversion is considered a sink of energy, whereas it is an energy source in the baroclinic energy equation. The conversion term is defined as:

$$C = \nabla_{\mathbf{h}} H \langle \mathbf{U} \, p_{bc}(-H) \rangle, \tag{10}$$

where $H$ is the bathymetry, $\mathbf{U} = (u_{bt}, v_{bt})$ the barotropic tidal velocity vector, and $p_{bc}$ the baroclinic tidal pressure at the ocean bottom $(-H)$. $\langle \rangle$ denotes the average over a tidal cycle. Following Zilberman et al. (2009), we compute $\langle \mathbf{U} \, p_{bc}(-H) \rangle$ via:

$$\langle \mathbf{U} \, p_{bc}(-H) \rangle = \frac{1}{2} \, A_{p_{bc}(-H)} \, A_{\mathbf{U}} \, \cos(\varphi_{p_{bc}(-H)} - \varphi_{\mathbf{U}}), \tag{11}$$

where $A$ and $\varphi$ are the respective amplitude and phase of the tidal harmonic obtained from $p_{bc}$ and $\mathbf{U}$. The conversion for each mode $n$ is given by:

$$C^n = \nabla_{\mathbf{h}} H \langle \mathbf{U} \, p_{bc}^n(-H) \rangle, \tag{12}$$

where $p_{bc}^n(-H)$ is the baroclinic pressure at the ocean bottom $(-H)$ for mode $n$. Equivalent to Equation 11, we compute for each mode $n$:

$$\langle \mathbf{U} \, p_{bc}^n(-H) \rangle = \frac{1}{2} \, A_{p_{bc}^n(-H)} \, A_{\mathbf{U}} \, \cos(\varphi_{p_{bc}^n(-H)} - \varphi_{\mathbf{U}}) \tag{13}$$

The propagation of barotropic and baroclinic tide energy is expressed by the energy flux ($\mathbf{F_{bt}}$ and $\mathbf{F_{bc}}$) and is considered here as a depth-integrated quantity:

$$\mathbf{F_{bt}} = \int_{-H}^{\eta} \langle \mathbf{U} \, p_{bt} \rangle \, dz, \tag{14}$$

$$\mathbf{F_{bc}} = \int_{-H}^{\eta} \langle \mathbf{u}\mathbf{u_{bc}} \, p_{bc} \rangle \, dz, \tag{15}$$

where $p_{bt}$ is the barotropic pressure, and $\mathbf{u_{bc}} = (u_{bc}, v_{bc})$ is the baroclinic velocity vector. The baroclinic energy flux for each mode $n$ is defined as:

$$\mathbf{F_{bc}^n} = \int_{-H}^{\eta} \langle \mathbf{u}^n{}_{\mathbf{bc}} \, p_{bc}^n \rangle \, dz, \tag{16}$$

where $\mathbf{u_{bc}^n}$ is the baroclinic velocity vector for mode $n$. Note that the average over a tidal cycle follows the same methodology as for the conversion term above. The barotropic ($D_{bt}$) and baroclinic ($D_{bc}$) dissipation is regarded as the residual of the energy flux divergence and conversion and, hence, obtained through Equation 8 and 9, respectively. As will be discussed later, $D_{bc}$ may contain both true baroclinic energy dissipation and scattering to the incoherent tide.

In the following, we mainly focus our study on the M2 semidiurnal tide which explains in the nesting domain more than 80 % of the total energy conversion from the barotropic to the baroclinic tide while representing about 84 % of the semidiurnal energy conversion (see Table 1).

**Table 1.** Full-domain, area-integrated barotropic-to-baroclinic conversion in GW for each tidal constituent (M2, S2, N2, K1, O1) with their respective contribution to the total in %.

| | Total | M2 | S2 | N2 | K1 | O1 |
|---|---|---|---|---|---|---|
| Conversion [GW] | 19.03 (100 %) | 15.27 (80.2 %) | 2.04 (10.7 %) | 0.92 (4.8 %) | 0.64 (3.4 %) | 0.16 (0.8 %) |

## 2.3 Other Data

### 2.3.1 CARS climatology and merged Argo-CARS velocity product

The model used in this study is being evaluated using climatology and observations. Model stratification and water masses vertical structure are evaluated using climatological hydrography data taken from the CSIRO Atlas of Regional Seas (CARS2009) that provides gridded maps of temperature and salinity by combining a variety of datasets (Ridgway et al., 2002, http://www.marine.csiro.au/~dunn/cars2009/). The large-scale regional mean circulation in the Coral Sea is compared to the Argo-CARS merged velocity product from Kessler and Cravatte (2013). This product derives absolute geostrophic currents using climatological hydrographic data from CARS2009 referenced to a level of known motion of 1000 m obtained by drifting trajectories of Argo floats.

### 2.3.2 Altimetry-derived EKE

Surface mesoscale eddy kinetic energy (EKE) during the period 2014-2018 is evaluated using global ocean gridded maps ($1/4°$) of SSH generated and processed by the E.U. Copernicus Marine Environment Monitoring Service (CMEMS, https://doi.org/10.48670/moi-00148). In detail, we use the multimission Data Unification and Altimeter Combination System (DUACS) product in delayed time and daily resolution with all satellite missions available at a given time. Mesoscale EKE was derived from the geostrophic velocity field as follows:

$$EKE = \frac{1}{2} \overline{u_g'^2 + v_g'^2}, \tag{17}$$

where

$$u_g = -\frac{g}{f} \frac{\partial \eta}{dy},$$

$$v_g = \frac{g}{f} \frac{\partial \eta}{dx},$$

$u_g = -\frac{g}{f}\frac{\partial \eta}{dy}, v_g = \frac{g}{f}\frac{\partial \eta}{dx}$ with $f$ the Coriolis parameter, $\eta$ the SSH above geoid (also referred to as absolute dynamic topography), and

$$(u_g', v_g') = (u_g - \overline{u_g}, v_g - \overline{v_g}),$$

$(u'_g, v'_g) = (u_g - \overline{u_g}, v_g - \overline{v_g})$ where the overbar denotes the temporal average over the period 2014-2018. Additionally, the geostrophic velocities were high-pass filtered at a cut-off period of 180 days to account for the mesoscale (Qiu and Chen, 2004). We computed the modeled EKE as closely as possible to the altimetric EKE.

### 2.3.3 In-situ mooring

245   As part of an assessment of the SARAL/altiKa satellite altimeter for the monitoring of the East Caledonian Current flowing along the Loyalty ridge, moorings and gliders have been deployed along the satellite ground track (Durand et al., 2017). Here, we take advantage of the current-meter mooring at 167.26° E, 20.44° W (about 30 km off the northern tip of Lifou Island in the core of the ECC; see Fig. 2a). The mooring was deployed from November 2010 to October 2011 at the bottom of the continental slope, in 3300 m water depth. It was equipped with an upward-looking LinkQuest FlowQuest 300 kHz ADCP (with 250   4 m bins) located at a mean depth of 80 m, and five RCM7 Aanderaa rotor current meters at 300, 400, 500, 600, and 1000 m. The mooring provided hourly records of the 1-min averaged ocean velocity over the upper 1000 m. Here, it is used to compare in-situ kinetic energy with the model (cf Sect. 3.3)

### 2.3.4 FES2014

The FES2014 global ocean tidal atlas (Lyard et al., 2021) is the latest release to improve tidal predictions based on the hydro-255   dynamic modeling of tides (Toulouse Unstructured Grid Ocean model, further denoted T-UGOm) coupled to an ensemble data assimilation code (spectral ensemble optimal interpolation, denoted SpEnOI). It is a very significant upgrade compared to the previous atlases, thanks to the improvement of the assimilated data accuracy and the model performance. FES2014 has been integrated in satellite altimetry geophysical data records (GDRs). It also provides very accurate open-boundary tidal conditions for regional and coastal modeling. Here, it is used to ensure the correct representation of the barotropic tide for SSH in both 260   the host and nesting grid.

### 2.3.5 HRET

The expression of internal tides in SSH in our model simulation is evaluated by the High Resolution Empirical Tide version 8.1 (HRET8.1, https://ingria.ceoas.oregonstate.edu/~zarone/downloads.html, Zaron, 2019; Carrere et al., 2021). The product uses essentially all exact-repeat altimeter mission data in the period 1992-2017 (TOPEX/Jason, Geosat, ERS, Envisat). In contrast 265   to other previous approaches, HRET differs by the subtraction of the mesoscale sea level anomaly from the SSH along the ground tracks. This ensures to have as little non-tidal variability as possible. This is followed by a harmonic analysis applied on a time series at each point along the ground track for missions with the same orbit.

### 2.3.6 Semi-analytical models of tidal energy conversion

Semi-analytical models have been developed to obtain a global estimate of energy conversion rates from the barotropic to 270   the baroclinic tide using bottom topography, climatological stratification, and tidal barotropic velocity (e.g. Nycander, 2005;

Falahat et al., 2014; Vic et al., 2019). Doing so, they are highly valuable for tidal mixing parameterizations in ocean and climate models that do not have the ability to explicitly resolve tidal processes (MacKinnon et al., 2017; de Lavergne et al., 2019, 2020). Here, we make use of the products from Falahat et al. (2014) and Vic et al. (2019) to evaluate our model energy conversion. At the same time, we emphasize the limited capability of semi-analytical models to accurately predict internal tide generation in shallow waters and in areas of complex bathymetry such as New Caledonia. Specifically, semi-analytical models break down for bathymetric slopes that are equal or larger than the internal tide wave slopes, i.e. critical to supercritical slopes. The wave ray-path slope $s$ is obtained from the dispersion relation as follows:

$$s = \sqrt{\frac{\omega^2 - f^2}{N^2 - \omega^2}}, \tag{18}$$

where $\omega$ is the tidal frequency. The buoyancy frequency $N$ is taken from near the ocean bottom. The steepness parameter $\alpha$, defined as the ratio of the seafloor topographic slope to the ray-path slope, qualifies the seafloor topography as subcritical ($\alpha < 0.8$ s), critical ($0.8$ s $\leq \alpha \leq 1.5$ s), and supercritical ($\alpha > 1.5$ s), following de Lavergne et al. (2019). Semi-analytical models are often corrected for energy conversion in the shallow waters due to violation of linear theory. Initially corrected for the upper 400 m in (Falahat et al., 2014) and the upper 700 m in Vic et al. (2019), we also correct Falahat et al. (2014) for the upper 700 m to ensure the best comparison among both products.

## 3   Model assessment

In the following, we will assess the model's capability to realistically reproduce motion from the large-scale circulation down to high-frequency motion while justifying the model's eligibility to simulate internal tide dynamics.

### 3.1   Mean circulation

The modelisation of the regional circulation in the Coral Sea represents a challenge due to the numerous islands that serve as obstacles forming boundary currents and westward jets as well as recirculation and eastward counter currents (Couvelard et al., 2008; Qiu et al., 2009). The main feature is a westward inflow from the South Pacific Subtropical Gyre which splits into strong zonal jets, western boundary currents, and eastward counter currents when encountering bathymetric features (Couvelard, 2007; Kessler and Cravatte, 2013; Cravatte et al., 2015; Qiu and Chen, 2004). The 2014-2018 mean, near surface (20-100 m) simulated velocity field (Fig. 2a) is compared to the Argo-CARS merged velocity (see Sect. 2.3.1 for a description, Fig. 2b). The model 5-year mean shows good agreement with the observed regional circulation. The westward zonal jets are well represented with the South Equatorial Current (SEC) being split into the North Vanuatu Jet (NVJ) and the North Caledonian Jet (NCJ) north of New Caledonia and the South Caledonian Jet (SCJ) south of New Caledonia. West of the main islands (New Caledonia, Vanuatu, Fiji), the observed surface eastward counter currents are also well simulated (Qiu et al., 2009). The circulation south of New Caledonia seems more variable, with less clearly defined mean currents in both products. There is evidence for the presence of the surface-intensified eastward Subtropical Counter Current (STCC) that emerges from the East Australian Current (EAC) recirculation (Ridgway and Dunn, 2003). It is clearly intensified in the model but the Argo-merged

product south of New Caledonia should be taken with caution since limited observations do not average out the signatures of ubiquitous mesoscale eddies. Overall, the mean circulation is well simulated, which is essential for the proper description of eddy-internal tide interactions being subject to Part II of this study.
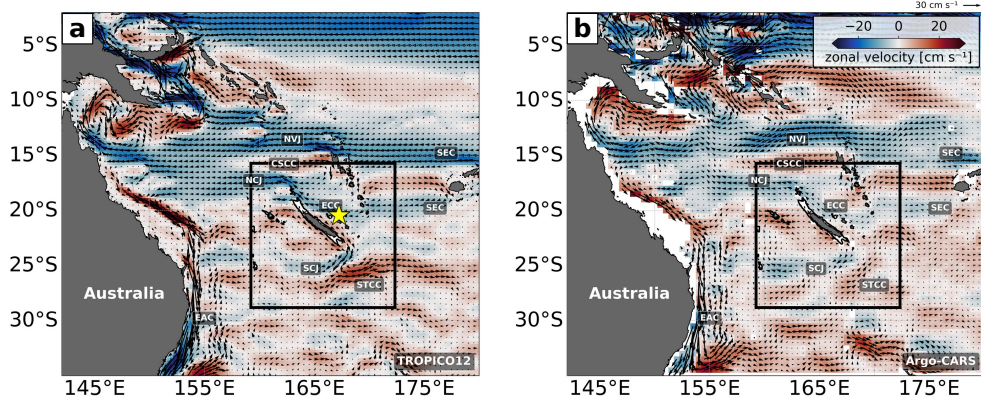
**Figure 2.** Coral Sea near-surface (20-100 m) regional circulation illustrating zonal velocity (shading) and velocity vectors from (a) TROPICO12 (2014-2018 mean) and (b) Argo-CARS merged velocity product (Kessler and Cravatte, 2013). The black box indicates the CALEDO60 domain. The major currents are labeled: South Equatorial Current (SEC), North Vanuatu Jet (NVJ), Coral Sea Counter Current (CSCC), North Caledonian Jet (NCJ), East Caledonian Current (ECC), South Caledonian Jet (SCJ), South Tropical Counter Current (STCC), and East Australian Current (EAC). The location of the in-situ mooring (cf Sect. 2.3.3) is indicated by the yellow star.
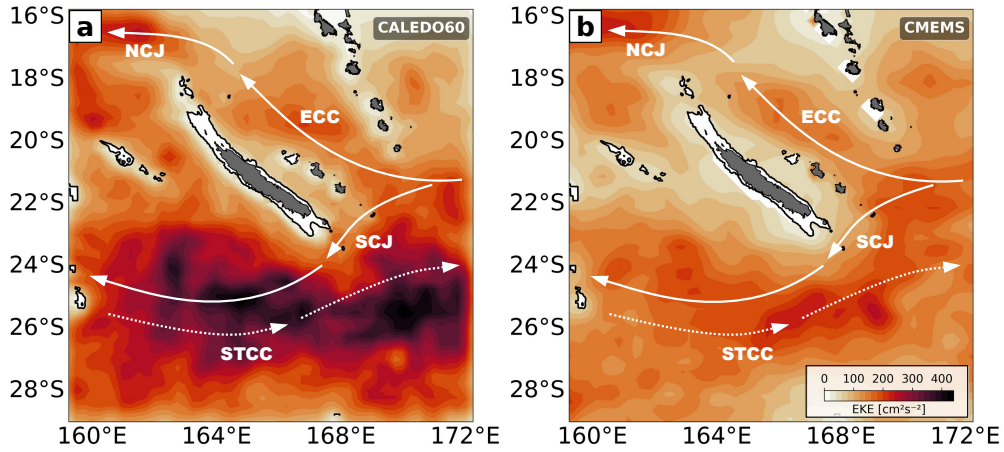
**Figure 3.** Surface mesoscale EKE derived from SSH for (a) CALEDO60 and (b) CMEMS altimeter products and averaged for the period 2014-2018. Currents are labeled as in Fig. 2.

## 3.2 Mesoscale variability

The large-scale circulation around New Caledonia is subject to barotropic and baroclinic instability of horizontally and vertically sheared currents (Qiu and Chen, 2004; Qiu et al., 2008, 2009) giving rise to mesoscale eddy variability. Here, the spatial pattern of the surface model mesoscale EKE (Fig. 3a) is compared to the mesoscale EKE as observed by satellite altimetry (Fig. 3b). We computed the modeled EKE as closely as possible to the altimetric EKE. To do so, we computed the 5-day mean of the model SSH to eliminate high-frequency variability such as tidal and inertial motions before horizontally binning the data onto the grid of present-day altimetry (1/4°). For proper comparison between model and altimeter observations, we also computed the 5-day average for altimetric SSH before the derivation of mesoscale EKE. Mesoscale EKE is maximum south of New Caledonia where mesoscale activity is expected to be generated through baroclinic instabilities of the vertically sheared SEC/SCJ-STCC currents (Qiu et al., 2009; Keppler et al., 2018). Elevated levels of EKE are also found along the eastern boundary current system between New Caledonia and Vanuatu and in the northwest of the domain through horizontal shear between the westward NCJ and the eastward Coral Sea Counter Current (Fig. 2, Fig. 3a). The spatial pattern of simulated EKE is in good agreement with satellite altimetry (Fig. 3b). Maximum levels of EKE in the southern domain where mesoscale activity is high are essentially lower than in the model ($> 250\,\mathrm{cm^2\,s^{-2}}$ compared to $> 400\,\mathrm{cm^2\,s^{-2}}$). We argue that this can be attributed to the present-day two-dimensional gridded satellite altimetry products. They are derived by gridding and optimal interpolation of available along-track SSH data, projected onto a 1/4°horizontal grid, and do not resolve wavelengths smaller than 150-200 km in our study region (Ballarotta et al., 2019). The model, even though gridded to 1/4°resolution, might contain dynamics that are associated with smaller scales.

## 3.3 Kinetic energy frequency spectra

In-situ observations are also used to validate energy levels from seasonal down to tidal frequencies obtained from a full-year in-situ current meter mooring (cf Sect. 2.3.3, Fig. 4). Model energy levels are very close to observations from seasonal to inertial timescales (180 days to 36 hours), i.e. for meso- and submesoscale processes. Inertial and tidal energy peaks are also in good agreement. For higher frequencies, the simulation with tidal forcing (red line) introduces a major improvement to the simulation without tidal forcing (blue line). This is especially true for the internal wave continuum raising the energy levels closer to the observations for frequencies $> f$. This validation, even if only performed at one location, gives us confidence in the ability of the numerical simulation to correctly represent the tides and their interaction with mesoscale processes.

Power spectral density of near surface (20-100 m) horizontal kinetic energy for CALEDO60 without (blue) and with (red) tidal forcing for the full model time series near 167.25 E, 20.43 S in the New Caledonian eastern boundary current (see Fig. 3a). The energy spectra are compared to a mooring time series that was deployed between November 2010 and October 2011 (Durand et al., 2017). The vertical dashed black lines are representative of the inertial frequency , the peak frequency of the K1 diurnal tide, and the peak frequency of the M2 semidiurnal tide. Note that the signal at the semidiurnal frequency (2 cpd) evident in the simulation with and without tides as well as in the mooring data is primarily linked to the atmospheric S2 tide which is contained in the atmospheric forcing of ERA5 (not shown; Chapman and Lindzen, 1969; Balidakis et al., 2022).

### 3.4 Barotropic M2 tide validation

The barotropic tide in both the host grid (TROPICO12) and the nesting grid (CALEDO60) is compared with the empirical
340    estimates from the barotropic tide model FES2014 (cf Sect. 2.3.4) by applying a harmonic analysis on the full-model hourly
SSH. Note that the daily output of the three-dimensional variables from TROPICO12 does not allow for a decomposition
between the barotropic and baroclinic tide through the projection onto vertical modes. Therefore, we treat the full-model SSH as
a proxy for the barotropic tide. For the sake of consistency, we do similarly for CALEDO60. The M2 tide of TROPICO12 (Fig.
5a) and CALEDO60 (Fig. 5c) are in overall accordance with FES2014 (Fig. 5c and Fig. 5d, respectively). The amphidromic
345    points are well located and amplitudes of SSH are of the same order of magnitude. Note that the modulations at shorter
wavelengths in Fig. 5c and Fig. 5d are attributed to the baroclinic SSH signature which are presented at later stage in Sect. 6.1.

### 3.5 Stratification

Finally, in order to study internal tide dynamics, a correct representation of the ocean's stratification is essential. Internal tide
350    express inter alia in the vertical displacement of isopycnal surfaces (Arbic et al., 2018) which can be decomposed by a sum of
discrete baroclinic modes that only depend on buoyancy frequency and water depth (cf Sect. 2.2.1). We compare the vertical
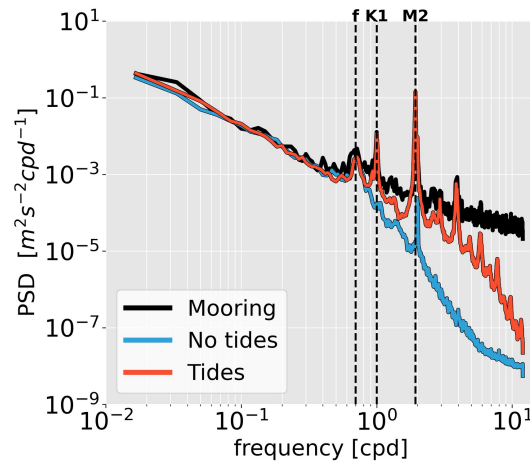
**Figure 4.** Power spectral density of near surface (20-100 m) horizontal kinetic energy for CALEDO60 without (blue) and with (red) tidal forcing for the full model time series near 167.25° E, 20.43° S in the New Caledonian eastern boundary current (see Fig. 3a). The energy spectra are compared to a mooring time series that was deployed between November 2010 and October 2011 (Durand et al., 2017). The vertical dashed black lines are representative of the inertial frequency $f$, the peak frequency of the K1 diurnal tide, and the peak frequency of the M2 semidiurnal tide. Note that the signal at the semidiurnal frequency (2 cpd) evident in the simulation with and without tides as well as in the mooring data is primarily linked to the atmospheric S2 tide which is contained in the atmospheric forcing of ERA5 (not shown; Chapman and Lindzen, 1969; Balidakis et al., 2022).
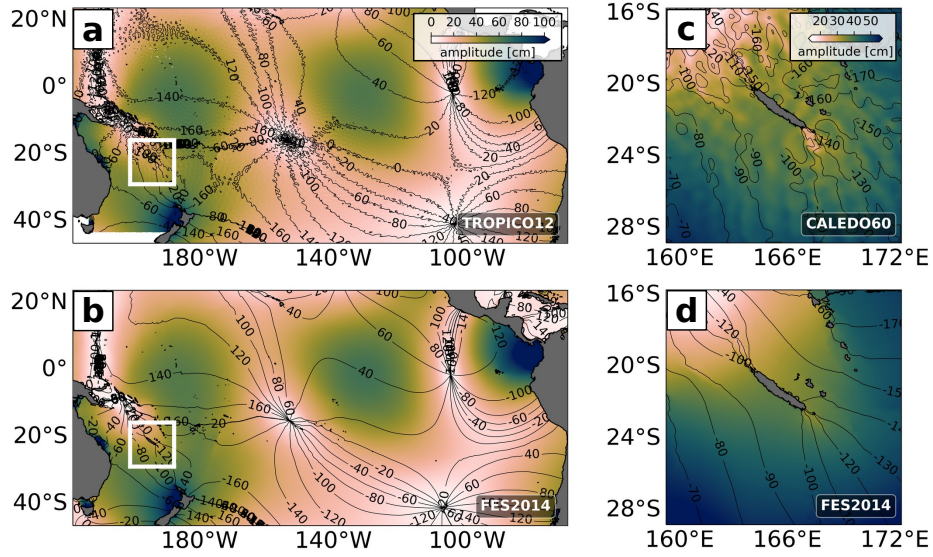
**Figure 5.** Barotropic M2 SSH amplitude (shading) and phase (contour) for (a) TROPICO12 and (c) CALEDO60 based on a 1-year (2014) harmonic analysis (assuming that the model SSH is dominated by the barotropic tide) and in comparison to the global tide atlas FES2014 for (b) TROPICO12 and (d) CALEDO60. The insets in (a) and (b) indicate the location of the CALEDO60 domain.

hydrographic structure of CALEDO60 with a hydrographic climatology (CARS2009, cf Sect. 2.3.1). The model mean density was horizontally binned to the climatological grid (1/2°), whereas the climatological density was vertically interpolated onto the model grid. The water masses (not shown) and buoyancy frequency profiles correspond well with each other. An example
355 of such comparison is illustrated by looking at a stratification profile south of New Caledonia (166° E, 26° S, Fig. 6a). The maximum stratification around 100 m depth is slightly reduced in the model compared to climatology. This is attributed to a reduced salinity maximum in the thermocline in the model (not shown). The normalized modal structures for the four lowest modes and for both the displacement and vertical velocity (Fig. 6b) agree well with climatology. In particular, the depth of the zero-crossings correspond well with each other.
360 Overall, we conclude that our model simulation is capable of realistically simulating both background ocean dynamics and internal tides. This encourages us to study in detail the internal tide field around New Caledonia including its tidal energy budget, its vertical structure, and finally its SSH signature.

## 4 Barotropic-baroclinic coherent M2 tide energy budget

In the following, we first analyze the M2 internal tide field around New Caledonia by quantifying the energy conversion from
365 the barotropic to the baroclinic tide while linking it with the local bathymetry. We also discuss the overall energy budget of the coherent M2 internal tide. We start with a regional overview before focusing on the regional hot spots of internal tide generation.
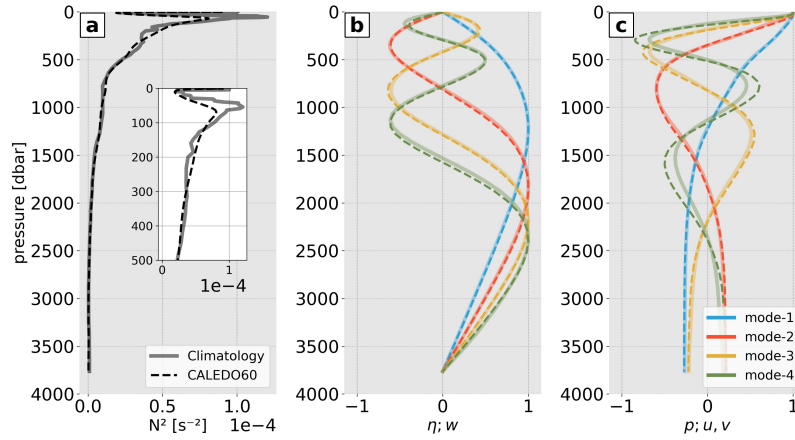
**Figure 6.** (a) Buoyancy frequency ($N^2$) for a representative profile at $166°$ E, $26°$ S from the CARS2009 climatology (solid) and CALEDO60 (dashed). A zoom for the upper 500 m is given in the inset. Normalized baroclinic modal structures for (b) displacement $\eta$ and vertical velocity $w$, and (c) pressure $p$ and horizontal velocity $u, v$ for the four lowest modes are also shown.

## 4.1 Regional overview

Tidal energy conversion from the barotropic to baroclinic tide is closely linked to the bathymetry that is shortly presented in the following for the regional model domain (Fig. 7a). It is characterized by a complex northwest-southeast extending ridge system, deep-reaching trenches, small-scale basins, seamounts, and shallow lagoons. The ridge system is composed of two major ridges, the Norfolk and Loyalty Ridge. The Norfolk Ridge extends from north of the Grand Passage all the way to the northern tip of New Zealand. The main New Caledonia island (Grande Terre) is located on the northern segment of the Norfolk Ridge, also referred to as the New Caledonia Ridge. The Loyalty Ridge stretches parallel to the Norfolk Ridge giving rise to the Loyalty Islands (Payri and de Forges, 2006). Seamounts are ubiquitous around New Caledonia, most prominent south of Grande Terre (Samadi et al., 2006).

~~CALEDO60 (a) bathymetry and (b) M2 tide slope ratio between topographic slope and wave slope , divided into subcritical (gray, < 0.8 s), critical (blue, 0.8 s < < 1.5 s), and supercritical (red, > 1.5 s) slopes. Note that white shaded grid points are associated with zero bathymetry gradient. The thin black lines represent the 1000 m, 2000 m, and 3000 m depth contours. The thick black line is the 100 m depth contour representative for the New Caledonian lagoon. The numbered, black boxes represent the hot spots of internal tide generation (1: North, 2: South, 3: Norfolk Ridge, 4: Loyalty Ridge) for which the distribution of slope ratio as a function of depth (divided into 200 m depth bins) is given in (c).~~

As the M2 barotropic tidal energy flux curves southwestward around New Caledonia, the region is subject to barotropic-to-baroclinic energy conversion (Fig. 8a). Positive conversions represent energy transfer from the barotropic to the baroclinic tide; negative conversion are argued to be a measure of the energy transfer from the baroclinic tide to the barotropic tide due to pressure work (Zilberman et al., 2009). However, they may also reflect limitations in the baroclinic/barotropic decomposition ~~(?)~~(Lahaye et al., 2020). Thus, they remain difficult to explain physically and will not be further discussed here.

In the full-model domain, a total 21.16 GW of barotropic tidal energy is lost, of which 72 % (15.27 GW) is transferred to baroclinic tidal energy, whereas 28 % (5.89 GW) is dissipated due to bottom friction. This is a significant loss of barotropic tidal energy. For comparison, barotropic tidal energy loss has been estimated at 18.35 GW and 2.73 GW of which 94 % and 84 % are converted to baroclinic tidal energy for the Luzon Strait (Kerry et al., 2013) and the Hawaiian Ridge (Carter et al., 2008), respectively.

In the whole domain (not shown), conversion is observed at all depths up to 4000 m and over a broad range of slopes. However, tidal conversion peaks in shallow waters with overall 25 % of the area-integrated energy that is associated with the upper 500 m. Moreover, two-thirds of the tidal conversion occurs on critical and supercritical slopes. Mode 1 clearly dominates, explaining almost 70 % of the total tidal energy conversion. Higher modes play only a minor role (15 % for mode 2, and 7 % for mode 3). For the whole domain, 93 % of this generated baroclinic energy is finally dissipated inside the domain, while only little
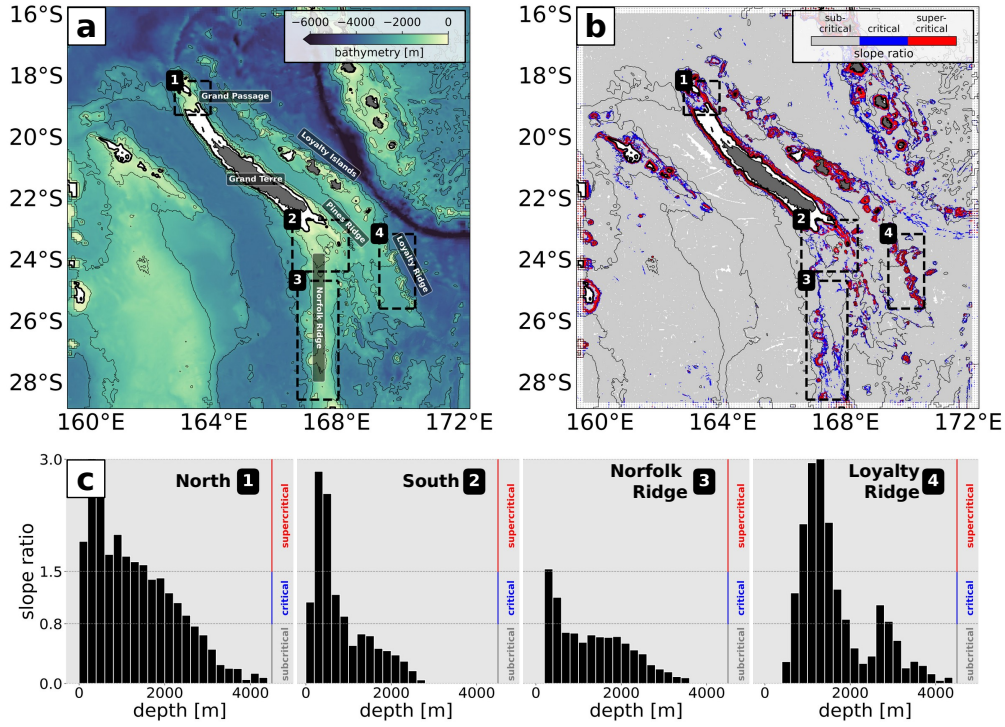
**Figure 7.** CALEDO60 (a) bathymetry and (b) M2 tide slope ratio $\alpha$ between topographic slope and wave slope $s$, divided into subcritical (gray, $\alpha < 0.8\,s$), critical (blue, $0.8\,s < \alpha < 1.5\,s$), and supercritical (red, $\alpha > 1.5\,s$) slopes. Note that white shaded grid points are associated with zero bathymetry gradient. The thin black lines represent the 1000 m, 2000 m, and 3000 m depth contours. The thick black line is the 100 m depth contour representative for the New Caledonian lagoon. The numbered, black boxes represent the hot spots of internal tide generation (1: *North*, 2: *South*, 3: *Norfolk Ridge*, 4: *Loyalty Ridge*) for which the distribution of slope ratio as a function of depth (divided into 200 m depth bins) is given in (c).

energy (1.06 GW) is leaving the domain (Fig. 8a). Note that this quantity is representative of the net baroclinic flux of inward and outward energy propagation.

## 4.2 Sub-regional analyses

Here, we identify four regions of internal tide generation which together represent roughly 60 % of the full-domain area-integrated M2 barotropic-to-baroclinic conversion. These hot spots are illustrated by the black boxes in Fig. 7a-b and Fig. 8a and defined as *North* (1), *South* (2), *Norfolk Ridge* (3), and *Loyalty Ridge* (4). The conversion and energy budget are discussed for each area in the light of its topographic characteristics (Fig. 7). The energy budget and the part dissipated locally is also provided for each sub-region to better infer where the dissipation occurs and where tidal mixing is expected (Fig. 9, see also Table A1).

The *North* (1) domain is characterized by a very steep (with critical and supercritical slopes) shelf break at the eastern flank of the New Caledonia Ridge and a 500 m deep, 50 km wide passage (Grand Passage) that is located between the d'Entrecasteaux Reef and the main island reef (Fig. 7a-b). Two-thirds of the tidal energy conversion occurs at depths shallower than 500 m (Fig. 8b), predominantly on critical and supercritical slopes (Fig. 7b-c). The region features the highest dissipation rate of barotropic energy compared to the other three regions. Of 3.83 GW that is lost by the barotropic tide, 1.66 GW (43 %) is directly lost
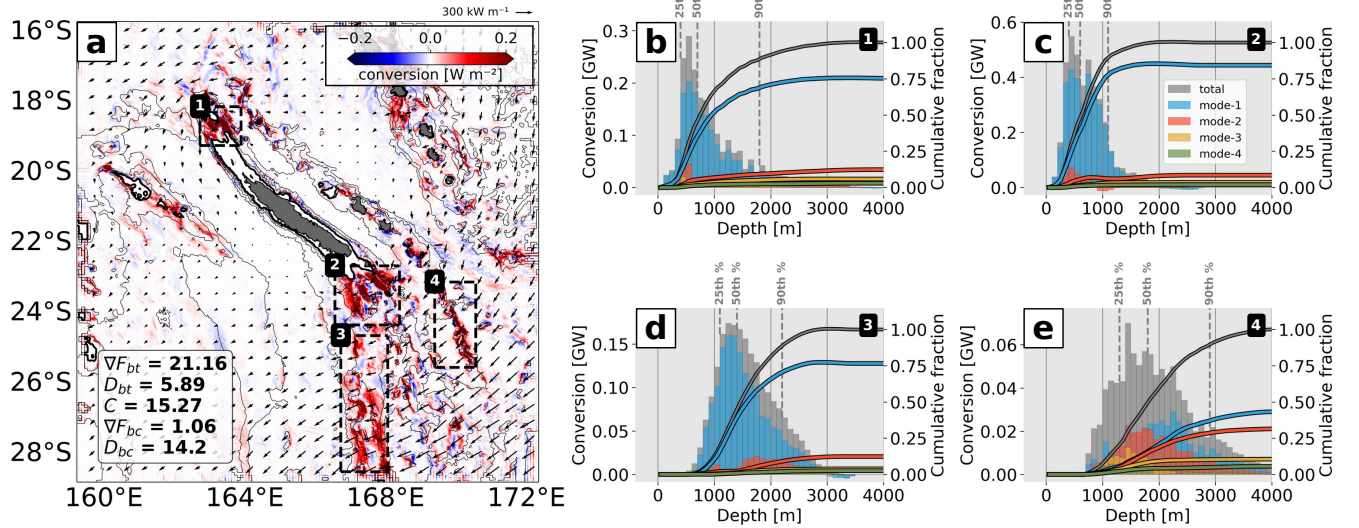
**Figure 8.** (a) M2 barotropic-to-baroclinic conversion including barotropic energy flux vectors and the full-domain area-integral of the barotropic energy flux divergence ($\nabla F_{bt}$), barotropic energy dissipation ($D_{bt}$), barotropic-to-baroclinic conversion ($C$), baroclinic energy flux divergence ($\nabla F_{bc}$), and baroclinic energy dissipation ($D_{bc}$) in GW. Bathymetry contours and the black boxes are given as in Fig. 7. Histograms of the regional area-integrated conversion (total baroclinic and four lowest modes) as a function of generation depth divided into 100 m depth bins for (b) *North* (1), (c) *South* (2), (d) *Norfolk Ridge* (3), and (e) *Loyalty Ridge* (4). The 25th, 50th, and 90th percentile as well as the normalized cumulative fraction are also shown.

through bottom friction (Fig. 9a). Of the 2.17 GW that is converted to baroclinic energy, 32 % (0.70 GW) dissipates locally while the remaining 68 % (1.47 GW) radiates away.

420  The *South* (2) domain has similar bathymetric characteristics in terms of depth and slopes. It represents the southward extension of the New Caledonia Ridge, just south of the New Caledonian lagoon. The most prominent bathymetric feature is the Pines Ridge: it is a very steep (critical and supercritical slopes) and narrow ridge (a few tens of km wide) of 100 km length that may be as shallow as 500 m (Fig. 7a-b). This regions will be analyzed in more detail in Sect. 4.5 since it is subject to the most intense energy conversion with a total of 3.92 GW (Fig. 9b), primarily in depths shallower than 500 m (Fig. 8c). Futher,

425  local dissipation is essentially higher than in the *North* (1) domain.

The *Norfolk Ridge* (3) exhibits different bathymetric characteristics. It is defined as the > 100 km wide north-south stretching
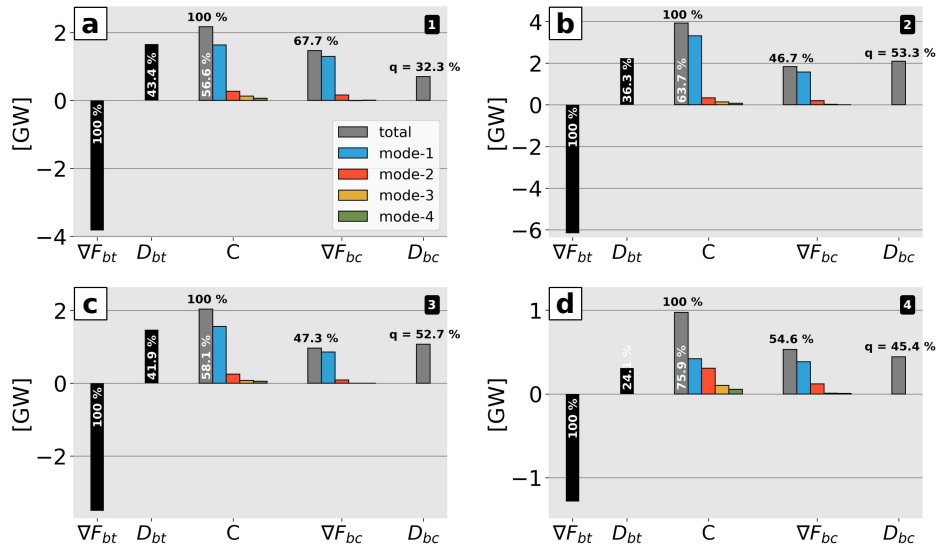
**Figure 9.** Bar plots of the regional barotropic-baroclinic M2 energy budgets for (a) *North* (1), (b) *South* (2), (c) *Norfolk Ridge* (3), (d) *Loyalty Ridge* (4) including the barotropic energy flux divergence ($\nabla F_{bt}$) and barotropic energy dissipation ($D_{bt}$) as well as conversion ($C$) and baroclinic energy flux divergence ($\nabla F_{bc}$) for the total baroclinic and the four lowest modes. The baroclinic energy dissipation ($D_{bc}$) determined by the residual of $\nabla F_{bc}$ and $C$ is also given. The percentage values (i) in white give the ratio of the barotropic energy flux divergence that is either dissipated through bottom friction or converted baroclnic energy and (ii) in black the ratio of the energy conversion term that is either radiated away or dissipated ($q$).

ridge between 24.5° S and 28.5° S. It is dominated by subcritical slopes at depths > 1000 m (Fig. 7c), and also features steep (critical) slopes at mid-depths (400-700 m) which are mostly associated with seamounts. It is mainly characterized by energy conversion at subcritical slopes peaking at depths in the range 1000-2000 m with the 50th % percentile at around 1500 m and
430 the 90th % percentile below 2000 m (Fig. 8d). Similarly to *South* (2), approximately half (53 %) of the converted baroclinic energy (2.04 GW) is dissipated locally (1.07 GW) while the other half (47 %) is radiated away (0.96 GW, Fig. 9c).

The *Loyalty Ridge* (4) is a deep and narrow ridge composed of seamounts and guyots (Pelletier, 2007). These seamounts and guyots are located between 1000-2000 m depth but deeper ones are also found between 2500-3000 m. They are characterized by supercritical and critical slopes, respectively (Fig. 7b-c). It features the most efficient energy conversion from the barotropic
435 to baroclinic tide. Of 1.28 GW that is lost by the barotropic tide, only 0.31 GW (24 %) is directly lost through bottom friction (Fig. 9d). The area-integrated baroclinic energy accounts for 0.97 GW of which 45 % dissipates within the region (0.44 GW) and 55 % leaves the domain (0.53 GW).

Most of the tidal energy conversion discussed above is dominated by mode 1 explaining 75 %, 84 %, 76 % for *North* (1), *South* (2), and *Norfolk Ridge* (3), respectively (Fig. 9a-c). In these, regions, mode 2 (7-12 %) and mode 3 (4-6 %) contribute
440 only little to the total baroclinic energy conversion. The *Loyalty Ridge* (4) represents an exception with notable contributions of higher vertical modes: 43 %, 31 %, 11 %, and 6 % associated with mode 1 through mode 4, respectively (Fig. 9d).

These findings are partly consistent with literature. In shallow depth ranges, the tidal energy conversion is expected to be largest for mode 1 (Falahat et al., 2014). Also, we expect mode 1 to be dominant for steep, tall, narrow structures such as in the *North* (1) and *South* (2) domains, similarly found for the Hawaiian Ridge (Laurent et al., 2003; Laurent and Nash, 2004). In case of
445 a deeper ocean bottom with small-scale bathymetric structures, such as the *Loyalty Ridge* (4), higher modes are expected to become more important. The general presence of critical and subcritical slopes suggests a superposition of numerous vertical modes forming beams (Gerkema, 2001; Balmforth et al., 2002; Legg and Huijts, 2006). Nevertheless, we did not find any clear relationship between the bathymetric slope and excitement of vertical modes. The high dissipation rates in *South* (2) and *Norfolk Ridge* (3) could be explained by the successive bathymetric obstacles encountered by the internal tide beams emanating
450 from the generation spots with low modes scattered to higher modes before being dissipated locally (?)(Lahaye et al., 2020). Surprisingly, the fraction of energy dissipation around *Loyalty Ridge* (4) is slightly reduced even though higher vertical modes are generated, which should imply more local dissipation.

Briefly summarized, the bulk of energy conversion from the barotropic to the baroclinic tide is confined to four hot spot regions in shallow waters (500 m), closely linked to the complex bathymetry (i.e. shelf breaks, ridges, and seamounts), and
455 dominated by mode 1. Approximately half of the locally generated energy dissipates locally in the near-field, whereas the other half propagates outside the hot spot regions. This suggests a quick attenuation of baroclinic energy. Our model results show that the fraction of coherent internal tides that loses energy locally ($q = D_{bc}/C$) is elevated in our study region compared to 36 % and 20 % for the Luzon Strait (Kerry et al., 2013) and the Hawaiian Ridge (Carter et al., 2008), respectively. Potential factors that may contribute to this loss of energy will be discussed later in Sect. 6.2. Particularly, we will point out that the high
460 dissipation rates observed in our analysis may not solely be associated with actual energy dissipation, but also with a loss of tidal coherence. This will be explored in more detail in Part II of this study.

### 4.3 Comparison with semi-analytical model estimates

In the following, we compare our M2 modal conversion for the four sub-regions with the semi-analytical model estimates from Falahat et al. (2014) (Falahat14) and Vic et al. (2019) (Vic19) in Fig. 10. Recall that both products represent here the energy conversion in depths > 700 m and on subcritical slopes only (cf Sect. 2.3.6). The model conversion is given for the full model (considering the full water column and subcritical, critical, supercritical slopes), the full model but only considering depths > 700 m, and the full model but only considering both depths > 700 m and subcritical slopes. The latter ensures the best comparison between the semi-analytical and numerical model estimates.

Overall, there is good agreement between our full model estimates and those from semi-analytical theory concerning the conversion's modal content with mode 1 being clearly dominant. Higher modes appear to only increase in relative importance for the *Loyalty Ridge* (4) (Fig. 10d). The full model energy conversion tends to be excessive in the *South* (2) domains (Fig. 10b). When correcting the full model for conversion in the upper 700 m in addition to conversion on critical and supercritical slopes, our model conversion compares better with the semi-analytical estimates. Even though corrected for the upper 700 , there is no good comparison with Vic19 in the *North* (1) domain (Fig. 10a). This could be related to violation of linear theory that leads to unrealistic conversion rates larger than the energy lost by the barotropic tide. Remaining discrepancies among the products may be attributed to the associated bathymetry products that differ in both horizontal resolution and the correct representation of those bathymetric structures that are key for internal tide generation.

While semi-analytical theory has proven very valuable in providing a first-order estimation of internal tide generation on global
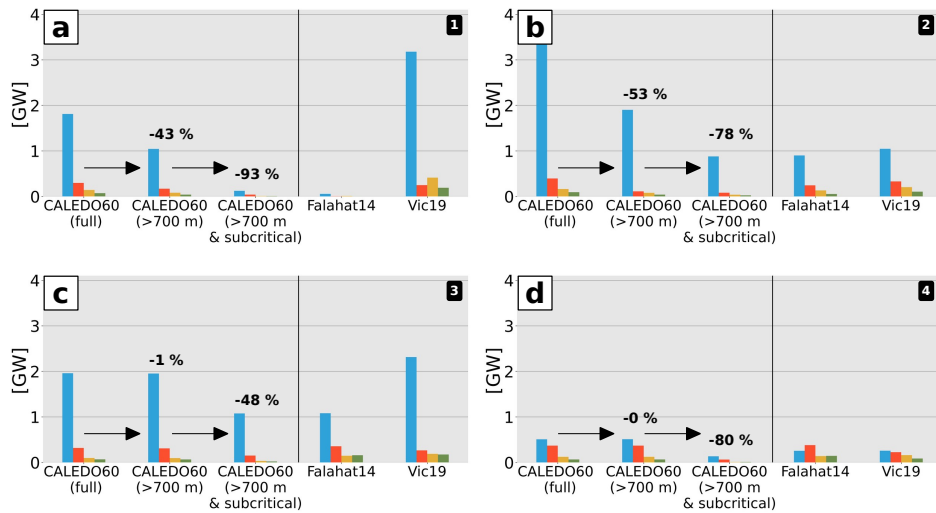
**Figure 10.** M2 barotropic-to-baroclinic energy conversion in GW for the four lowest modes integrated over (a) *North* (1), (b) *South* (2), (c), *Norfolk Ridge* (3), and (d) *Loyalty Ridge* (4) for the full model, corrected for the upper 700 m, and corrected for both the upper 700 m and critical to supercritical slopes. The associated percentage decrease for the given correction is also shown. Energy conversion is compared to the semi-analytical estimates from Falahat et al. (2014) (Falahat14) and Vic et al. (2019) (Vic19) corrected for the upper 700 m.

scales, they reach their limits in regions with shallow and complex bathymetry with critical to supercritical slopes. In fact, we find for the sub-regions around New Caledonia that roughly 50-90 % of the energy conversion may be missed locally when not allowing for conversion in the upper 700 m and on critical to supercritical slopes. This highlights the need for realistic, high-resolution numerical simulations to more faithfully represent the local internal tide generation and dynamics.

~~M2 barotropic-to-baroclinic energy conversion in GW for the four lowest modes integrated over (a) *North*, (b) *South*, (c), *Norfolk Ridge*, and (d) *Loyalty Ridge* for the full model, corrected for the upper 700 m, and corrected for both the upper 700 m and critical to supercritical slopes. The associated percentage decrease for the given correction is also shown. Energy conversion is compared to the semi-analytical estimates from Falahat et al. (2014) (Falahat14) and Vic et al. (2019) (Vic19) corrected for the upper 700 m.~~

### 4.4 Regional overview of tidal energy propagation and dissipation

The propagation of baroclinic tidal energy expresses mainly by two predominant tidal beams that emerge from the *North* (1) and *South* (2) domains (Fig. 11a). They are 100-200 km in width, feature magnitudes well above 20 kW m$^{-1}$ (locally up to 30 kW m$^{-1}$) near the respective generation sites, but propagate not more than 800 km toward the open ocean. In contrast to the southern tidal beam that propagates from its generation site at the Pines Ridge southwestward and northeastward (though the northeastward beam is more limited), the northern tidal beam mainly propagates northeastward. This is attributed to the energy conversion that is confined to the shelf break east of the Grand Passage, whereas the Grand Passage itself is subject to only minor energy conversion (not shown). Tidal beams also emerge from the *Norfolk Ridge* (3) and *Loyalty Ridge* (4). However, they are overall less pronounced and smaller in magnitude (5 kW m$^{-1}$).

The rather quick attenuation of ~~baroclinic energy, shown by the~~ the tidal beams may be associated with the high dissipation
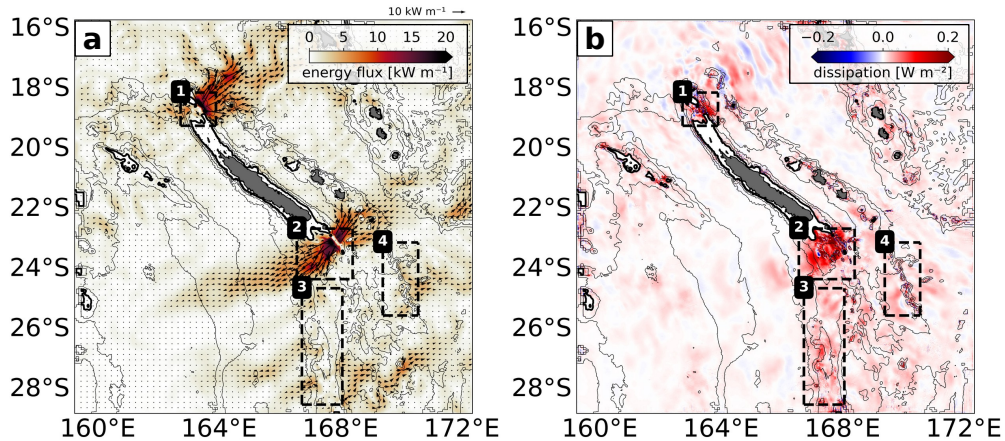
**Figure 11.** (a) M2 coherent energy flux (shading) including flux vectors. (b) M2 coherent energy dissipation (residual between the energy flux divergence and conversion). Bathymetry contours and the black boxes are given as in Fig. 7.

rates~~(residual between baroclinic energy flux divergence and conversion) is particularly evident in~~ , which are to a large part constrained to the hot spot regions (Fig. ~~9 and Fig.~~ 11b). ~~Our model results show that the fraction of coherent internal tides that~~ ~~loses energy locally ($q = D_{bc}/C$) is elevated in our study area (~~This is reflected in the regional energy budgets and sheds light on the high fraction ($\sim$ 50 %) ~~compared to 36 % and 20 % for the Luzon Strait (Kerry et al., 2013) and the Hawaiian Ridge~~ ~~(Carter et al., 2008), respectively. Potential factors that may contribute to this loss of energy will be discussed later in Sect. 6.2,~~ ~~and are further explored in Part II of this study.~~between local energy dissipation and generation (cf Sect. 4.2). Dissipation also occurs away from the hot spot regions, but to a lower degree.

~~(a) M2 coherent energy flux (shading) including flux vectors. (b) M2 coherent energy dissipation (residual between the~~ ~~energy flux divergence and conversion). Bathymetry contours and the black boxes are given as in Fig. 7.~~

## 4.5 Zoom in the *South* (2) domain

The *South* (2) domain deserves special attention for two reasons: First, it represents a study area of the SWOT-AdAC program accompanied by an extensive field campaign. This will be further addressed in Sect. 6.4. Second, it represents the predominant
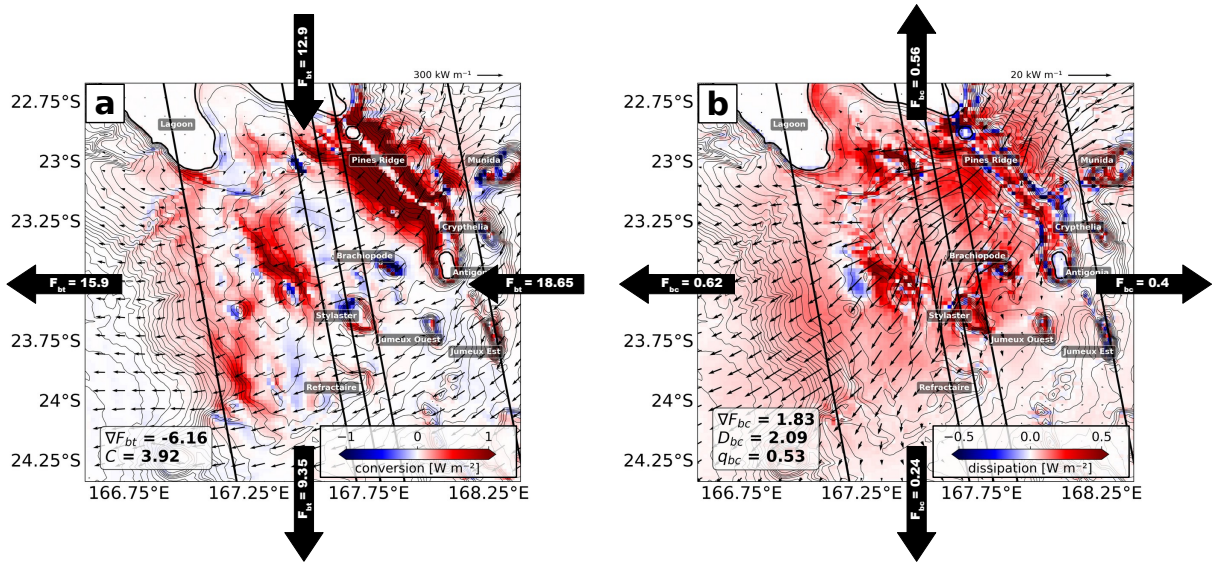
**Figure 12.** Regional M2 energy budget for the *South* (2) domain showing (a) the barotropic-to-baroclinic conversion (shading) overlaid by the barotropic energy flux (vectors) and (b) the depth-integrated baroclinic energy dissipation overlaid by the depth-integrated baroclinic energy flux (vectors). The area-integrated values for the barotropic energy flux divergence ($\nabla F_{bt}$) and barotropic-to-baroclinic conversion $C$ in (a) and the baroclinic energy flux divergence ($\nabla F_{bc}$), the baroclinic energy dissipation $D_{bc}$, as well as the ratio of locally dissipated baroclinic energy $q_{bc}$ in (b) are also given. The incoming/outgoing (a) barotropic and (b) baroclinic energy flux with integrated values along the boundary are illustrated at the lateral boundaries of the domain indicating the net direction of energy propagation. All integrated quantities are given in GW. The Pines Ridge, the lagoon and the most prominent seamounts are labeled. The depth contour interval is 100 m. The SWOT swaths and nadir track (solid black lines) during the fast-sampling phase (1-day repeat orbit) are also shown.

510     hot spot of internal tide generation contributing by more than 40 % and 25 % to the area-integrated barotropic-to-baroclinic energy conversion associated with the four sub-regions and full regional domain, respectively.

In total, 6.16 GW are lost by the barotropic tide of which 64 % (3.92 GW) are converted to internal tides (Fig. 12a). The bulk of energy is generated when the incoming barotropic tidal flow encounters the Pines Ridge featuring conversion rates well above 1 W m$^{-2}$ on both its western and eastern flanks. Further internal tide generation is localized downstream along

515     a secondary ridge parallel to the Pines Ridge and across the western shelf break. Locally, positive conversion is also evident around seamounts that are present in the area, namely, Munida, Antigonia, Jumeux Est, and Stylaster.

In contrast to the conversion map which shows isolated spots, baroclinic energy dissipation is observed throughout the domain, accounting for a total of 2.09 GW (Fig. 12b). In other words, well above 50 % of the locally generated energy dissipates within the *South* (2) domain. Dissipation maxima are located near the generation sites such as Pines Ridge and around the

520     seamounts with dissipation rates > 0.5 W m$^{-2}$, i.e. around Munida, Brachiopode, Jumeux Ouest, and Stylaster. Increased levels of dissipation are also found along the barrier reef that encloses the South Caledonian lagoon. Further energy dissipation occurs uniformly westward and eastward of the Pines Ridge across the shelf break with constant dissipation rates > 0.1 W m$^{-2}$. The non-dissipated energy propagates away from the main generation site within well-confined tidal beams in southwestern and northeastern directions characterized by energy fluxes > 20 kW m$^{-1}$ which attenuate gradually to roughly 10 kW m$^{-1}$

525     within 100 km distance to the generation site in the annual mean. A net energy flux of 1.83 GW leaves the *South* (2) domain accounting for 47 % of the locally generated baroclinic tidal energy.

## 5   Internal tide SSH signature

The expression of internal tides in SSH is of major interest for SWOT observability of meso- to submesoscale dynamics. Here, we first investigate the M2 tide amplitude around New Caledonia before addressing the tidal signature in spectral space.

530     The questions of interest are: 1) What are the processes that dominate in our study region the SSH signal in the meso- to submesoscale range? 2) What is the contribution of the coherent internal tide to these SSH signals? 3) To what extent are we able to increase observability of the meso- to submesoscale when correcting for the coherent internal tide?

### 5.1   SSH amplitude of the M2 internal tide around New Caledonia

We present the spatial maps of mode 1 and mode 2 of the M2 SSH amplitude in Fig. 13a and Fig. 13b in comparison with the

535     satellite altimetry derived empirical estimates from the HRET model (cf Sect. 2.3.5) in Fig. 13c and Fig. 13d for mode 1 and mode 2, respectively. Dominated by mode 1, the spatial distribution of SSH reveals multiple interference patterns with M2 tidal waves emanating from multiple generation sites and summing constructively and destructively as they propagate (Fig. 13a). Amplitudes may reach more than 6 cm in the internal tide hot spot regions. Following a similar pattern but strongly reduced in amplitude, mode 2 features significant amplitudes of up to 2 cm at some locations. Overall, the M2 SSH signature resembles

540     the energy flux in Fig. 11a with the predominant tidal beams to the north and south of New Caledonia. There is good agreement with the HRET model concerning the spatial representation of the M2 SSH for both mode 1 (Fig. 13c) and mode 2 (Fig. 13d).

Overall, mode 1 seems to be enhanced in our model, whereas mode 2 is underestimated in some regions. Note that the given differences may be associated with the different time periods the datasets are referenced to as well as the length of the time series for the model (1 year) and altimetry (25 years).
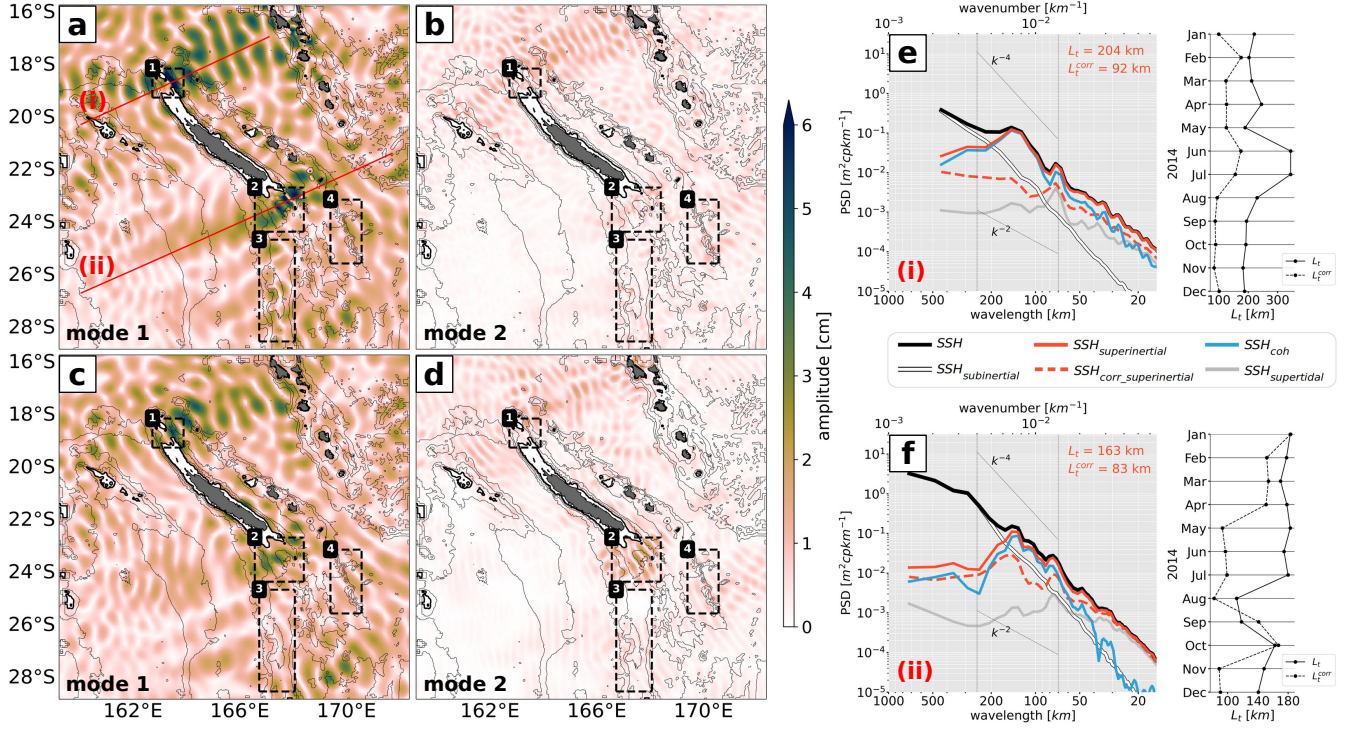
**Figure 13.** CALEDO60 M2 SSH amplitude for (a) mode 1 and (b) mode 2 in comparison with the empirical estimates of the High Resolution Empirical Tide (HRET) model for (c) mode 1 and (d) mode 2. Bathymetry contours and the black boxes are given as in Fig. 7. Annually averaged SSH wavenumber spectra for two transects (e) north and (f) south of New Caledonia, denoted (i) and (ii) respectively in (a) (red lines). SSH spectra are presented for the altimetry-like SSH (corrected for the barotropic tide, $SSH$, black) with regard to the different dynamics that are separated in terms of frequency bands: subinertial ($\omega < f$, $SSH_{subinertial}$, white) for meso- and submesoscale dynamics, superinertial frequencies ($\omega > f$, $SSH_{superinertial}$, solid red) for internal gravity waves decomposed into the coherent ($SSH_{coh}$, blue) internal tide and supertidal frequencies ($\omega > 1/10$ h, $SSH_{supertidal}$, gray). The altimetry-like SSH corrected for both the barotropic and baroclinic tide and filtered for motions at superinertial frequencies ($SSH_{corr\_superinertial}$, dashed red) is also given. The characteristic wavenumber slopes $k^{-2}$ and $k^{-4}$ are represented by the dotted black lines encompassing the mesoscale band (70-250 km, vertical dotted black lines). The transition scale $L_t$ (i.e. where $SSH_{superinertial} > SSH_{subinertial}$) and the transition scale corrected for $SSH_{coh}$ ($L_t^{corr}$, i.e. where $SSH_{corr\_superinertial} > SSH_{subinertial}$) for the annually averaged SSH spectra are specified by the red colored numbers. The right panels of (e) and (f) show the monthly evolution of $L_t$ (solid) and $L_t^{corr}$ (dashed).

## 5.2 SSH spectral signature

Wavenumber SSH spectra are commonly used to investigate dynamical regimes at work, and to explore the relative importance of balanced and unbalanced motions which may feature similar wavelengths: the wavenumber slopes and relative levels of variance both provide information on these issues ~~(e.g. Le Traon et al., 2008; Dufau et al., 2016; ?; Tchilibou et al., 2020, 2022; Vergara et al.,~~ (e.g. Le Traon et al., 2008; Dufau et al., 2016; Savage et al., 2017; Tchilibou et al., 2020, 2022; Vergara et al., 2022, and many more).

Here the objective is to describe for two given transects in tidal beam direction (red lines in Fig. 13a) the SSH signature with regard to the different dynamics that are separated in terms of frequency bands: subinertial frequencies ($\omega < f$, $SSH_{subinertial}$) for meso- and submesoscale dynamics, superinertial frequencies ($\omega > f$, $SSH_{superinertial}$) for internal gravity waves while distinguishing between the coherent internal tide ($SSH_{coh}$) and supertidal frequencies ($\omega > 1/10$ h, $SSH_{supertidal}$).

Further, we will examine how SWOT observability may be limited in a region with strong internal tides. SWOT observability of meso- and submesoscale dynamics (balanced motion in this case) is ultimately governed by the transition scale $L_t$ that separates balanced from unbalanced motion. The transition scale is a quantitative measure to estimate above which scales in spectral space the geostrophic balance is valid to derive balanced motion. Here, we define it as the intersection of subinertial and superinertial spectra. In other words, the transition scale is set to wavelengths where subinertial variance equals superinertial variance.

For both regions, subinertial processes explain almost all of the SSH variance for scales larger than 200 km (Fig. 13e and Fig. 13f). For scales smaller than 200 km, SSH variance is governed by superinertial processes which are largely dominated by the coherent internal tide clearly expressed in spectral space with mode 1 and mode 2 around 160 km and 80 km wavelength. In the annual mean, $L_t$ is set to (i) 204 km and (ii) 163 km meaning that the observability of balanced motion is largely limited below these scales as unbalanced motion dominates the SSH variance.

The correction of the total SSH for the coherent internal tide may be a promising attempt to assess balanced SSH dynamics. Doing so, $L_t$ reduces (i) from 204 km to 92 km and (ii) from 163 km to 83 km. The right panels of Fig. 13e and Fig. 13f show the monthly evolution of $L_t$ and the corrected transition scale $L_t^{corr}$ over one model year. Temporal variations of the ~~variations of the~~ transition scale may be the result of the relative importance of subinertial motion which undergoes seasonal variability. This was explicitly shown for New Caledonia by Sérazin et al. (2020) where the authors attributed the increasing importance of mixed layer instabilities and frontogenesis to more available potential energy in the southern hemisphere winter months. Other temporal variations of the transition scale may be related to temporal variability of the internal tide. The coherent internal tide is by definition constant, but the incoherent internal tide (not shown here) depends on the seasonally-varying stratification ~~(?)~~ (Lahaye et al., 2019) and/or the interaction with the background currents (see Sect. 1 for references). Moreover, the incoherent signal remains in the corrected SSH signal. Therefore, the extent to which we can increase observability of meso- and submesoscale dynamics in areas with internal tide activity depends on the amplitude of the incoherent internal tide. The characterization of the incoherent internal tide and its implications for SWOT SSH measurements is beyond the scope of this paper's objective, but it will be specifically addressed in Part II.

Briefly, the dominance of unbalanced motion in the meso- to submesoscale band strongly restricts SSH observability of geostrophic dynamics to large eddy scales in our study regions. However, a correction for the coherent internal tide may improve the observability to well below 100 km.

## 6 Summary and discussion

Prominent topographic structures such as oceanic ridges, continental shelf breaks, seamounts, and island chains give rise to major internal tide formation in large parts of the Pacific Ocean (Niwa and Hibiya, 2001). The majority of recent studies on internal tides focused mainly on two regions: the Luzon Strait (e.g. Niwa and Hibiya, 2004; Alford et al., 2011; Kerry et al., 2013) and the Hawaiian Ridge (e.g. Merrifield and Holloway, 2002; Zaron and Egbert, 2006; Carter et al., 2008). Here, we present for the first time the internal tide dynamics around New Caledonia in the Southwestern Tropical Pacific Ocean, using the output of a tailored high-resolution regional numerical model. Being subject to strong internal tides and elevated mesoscale eddy activity, New Caledonia represents an area of high interest for the upcoming SWOT altimeter mission to evaluate observability of meso- and submesoscale dynamics in the presence of unbalanced motion at wavelengths of similar scale. This is primarily true for the SWOT fast-sampling phase, when the satellite samples every day this region of interest. In this context, a dedicated field campaign (SWOTALIS, March-April 2023) was carried out in the framework of the SWOT AdAC program (Morrow et al., 2019; d'Ovidio et al., 2019). The model results we obtained provide new and key information for the New Caledonia study region, but also more globally for the understanding of the generation and life cycle of internal tides. We were also able to gain insights into SWOT observability in a challenging region with strong internal tidal waves. These findings are summarized and discussed below.

### 6.1 New Caledonia: a hot spot of mode-1 internal tide generation in the Pacific

The barotropic and baroclinic energy budget of the dominant M2 tide shows that in the regional model domain surrounding New Caledonia, 21.16 GW of the barotropic tidal energy is lost of which 72 % (15.27 GW) is converted into baroclinic tidal energy. The main conversion zones are associated with the most prominent bathymetric structures such as the Grand Passage (2.17 GW) and Pines Ridge (3.92 GW), north and south of New Caledonia, respectively. This confirms that New Caledonia is a hot spot of internal tide generation. The amount of energy converted is comparable to what has been estimated in the Luzon Strait (Kerry et al., 2013) and the Hawaiian Ridge (Carter et al., 2008), taking into account that the exact numbers depend on the size of the domain. The area-integrated M2 conversion is estimated as 15.27 GW around New Caledonia, 16.97 GW in the Luzon Strait, and 2.34 GW along the Hawaiian Ridge. Conversion integrated in the smaller sub-regions *North* (1) and *South* (2) are similar to the Hawaiian Ridge (2.17 GW and 3.92 GW, respectively). Local conversion rates are of the same order of magnitude (well above 1 W m$^{-2}$) among all regions. Further, all regions feature similar energy propagating away from the formation site within well-defined tidal beams. Maximum M2 baroclinic energy fluxes vary from 10 kW m$^{-1}$ at the Hawaiian Ridge, up to 30 kW m$^{-1}$ around New Caledonia, and 40 kW m$^{-1}$ at the Luzon Strait.

Interestingly, the New Caledonia region stands out compared to other previously studied regions in terms of modal content. Our

modeling results suggest that barotropic tidal energy is converted, overwhelmingly, into baroclinic mode-1 (75 % of the full-domain energy conversion, and up 85 % in the *South* (2) domain). Modes 2-4 represent a comparable amount of energy only at the *Loyalty Ridge* (4) characterized by deep topography. For comparison, this mode-1 conversion percentage was estimated to be around 30 % at global scale, 35 % for the Pacific basin (Falahat et al., 2014; Vic et al., 2019), 30 %-60 % around Hawaii (Merrifield and Holloway, 2002; Zilberman et al., 2011), and about 9 % over the Northern Atlantic Ridge (Vic et al., 2018). The reasons behind this strongly dominant mode 1 were not completely understood. A dominance of mode 1 in the western Pacific had been suggested previously with semi-analytical models (Falahat et al., 2014; Vic et al., 2019), but not to that extent. Mode 1 has been suggested to be dominantly generated in shallow depths (Falahat et al., 2014). Apart from topographic characteristics such as height, width, and depth (Legg and Huijts, 2006; Falahat et al., 2014), the modal content is argued to be primarily governed by roughness and, thus, by the topography's spectral shape (Laurent and Nash, 2004). On the other hand, it has been observed and argued by many that critical and supercritical slopes are conducive to beam-like patterns, requiring the presence of higher vertical modes (Gerkema, 2001; Balmforth et al., 2002; Legg and Huijts, 2006). Fully understanding the strong dominance of mode 1 in our region characterized by the presence of steep, tall, and shallow ridges with critical and supercritical slopes, and 25 % of the conversion taking place above 500m, would require further analyses.

An important lesson learned is that New Caledonia represents a complex area for linear semi-analytical models that break down for critical and supercritical slopes and shallow bathymetry which in turn are key for internal tide generation at our study site. Such semi-analytical models, although very useful and widely used to estimate tidal energy conversion, its modal distribution, and tidal mixing (e.g. Falahat et al., 2014; Vic et al., 2019; de Lavergne et al., 2019, 2020), miss a significant part of the conversion (50-90 %) in our area, pointing out the limitation of these approaches in such complex areas. This issue was also presented in Buijsman et al. (2020). However, it was only addressed on global scales highlighting here the relevance of realistic numerical simulations on regional scales.

## 6.2 A hot spot of internal tide dissipation

Our model results suggest elevated ratios ($q$) between local tidal energy dissipation and generation of $\sim 50$ % compared to other internal tide generation hot spots in the Luzon Strait (36 %, Kerry et al., 2013) and the Hawaiian Ridge (20 %, Carter et al., 2008). This is surprising considering the clear dominance of mode 1 in most parts of our nesting model domain where mode 1 dominates the baroclinic tidal energy propagation. Nonetheless, the elevated levels of local energy dissipation provide an explanation for the relatively small propagation distance of the tidal beams (e.g. around ~~700~~800 km for the tidal beam emanating from *South* (2), essentially smaller compared to the tidal beams emanating from the Luzon Strait and the Hawaiian Ridge that may propagate several thousands of km toward the open ocean. Several processes of tidal energy dissipation have been discussed in literature, well summarized in de Lavergne et al. (2019, 2020): non-linear wave-wave interactions, wave breaking through shoaling, dissipation on critical slopes, and scattering by abyssal hills. The interaction with the the topography may explain a largest fraction of energy dissipation (Kelly et al., 2013). This concerns especially the scattering/energy transfer of the low-mode internal tide to higher modes leading to increasing dissipation. Non-linear wave-wave interactions were shown to facilitate the energy transfer of low-mode internal tides to both superharmonic (Baker and Sutherland, 2020;

645 Sutherland and Dhaliwal, 2022) and subharmonic frequencies (Ansong et al., 2018; Olbers et al., 2020). Particularly, the latter which is associated with parametric subharmonic instability can be an important energy sink for low-mode internal tides near the critical latitude band (around 29° N/S for the semidiurnal tide) south of New Caledonia. The mechanisms of tidal energy dissipation and their relative contributions in our study area remain an open question. This is beyond the scope of this study and requires further investigation.

650 Recall that here the ~~dissipation~~ tidal energy dissipation (residual between energy flux divergence and conversion) corresponds to a coherent tidal analysis. Due to the length of the harmonically analyzed time series (full-model calendar year), it must be assumed that a non-negligible fraction of the coherent dissipation is not associated with true dissipation but with a loss of coherence or scattering of energy to the incoherent tide, i.e. with increasing distance from the internal tide generation site (Rainville and Pinkel, 2006; Alford et al., 2019). ~~This~~ The actual fraction of true energy dissipation will be addressed in more
655 detail in Part II of this study involving the full semidiurnal signal and tidal incoherence. A potentially important contribution to elevated dissipation rates could also be linked to the chosen bottom friction/drag parameterization (cf Sect. 2.1). The tidal dissipation's sensitivity to the given parameterization, however, was not addressed and would require a dedicated analysis.

### 6.3  A challenging spot for SWOT observability

660 The SWOT mission is dedicated to document two-dimensional fine-scale features down to 15 km wavelength that include both subinertial (meso- to submesoscale dynamics) and superinertial (such as internal tides) frequencies. Disentangling these different dynamics in terms of SSH is of interest for SWOT observability. Here, we have investigated the transition scale that separates the larger scale dominated by balanced geostrophic motion from the smaller scale dominated by unbalanced wave motions in the two main pathways of the internal tide energy flux. Further, we analyzed what impact the correction for the
665 coherent tide in the SSH signal has on the transition scale.

Wavenumber spectra of SSH reveal the dominance of unbalanced, rapidly-changing motion, largely governed by the internal tide, in the mesoscale band at spectral wavelengths below 200 km. The separation length scale between balanced and unbalanced motion is in good agreement with estimates deduced from along-track satellite altimetry in Vergara et al. (2022, see their Fig. 6). Our findings also align with the global model analysis from ~~?~~Qiu et al. (2018), where the SSH-derived transition scale
670 is estimated to be slightly below 200 km and 160 km north and south of New Caledonia, respectively.

Correcting our model for the coherent internal tide, we are able to improve the observability of meso- and submesoscale SSH around New Caledonia to well below 100 km in the annual mean. The limited observability even after the correction of the coherent internal tide is potentially linked to the temporally varying tide. The study region may be subject to strong interactions between internal tides and mesoscale eddies giving rise to tidal incoherence. This is especially true south of the New Caledonia
675 that is characterized by elevated levels of EKE (cf Fig. 3).

## 6.4 Perspectives of this work

This work is a first modeling approach to characterize the internal tide dynamics around New Caledonia. Part I focuses on the coherent part of the main M2 component. Giving first insight into internal tide generation, propagation, and dissipation as well as SSH observability, this study is meant to serve as a basis for future studies such as eddy-internal tide interactions and their expression in SSH. Internal tides may be strongly sensitive to the background currents, both at the generation sites and along propagation with implications for tidal energy conversion from the barotropic to baroclinic tide and tidal energy dissipation. This will be subject to Part II of this study. Further, a twin simulation experiment, with the same forcing and parameterizations, but without tidal forcing, has been performed. Comparing both simulations will help understand how tides impact the meso- and submesoscale fields, and the forward and inverse energy cascades among spatial scales (work in progress).

The results obtained will play an important role when confronted to in-situ observations. The dedicated SWOTALIS in-situ experiment has been carried out in March-May 2023 during the SWOT fast-sampling phase (related to SWOT-AdAC) beneath the SWOT swaths and nadir track. Observational platforms such as moorings, repeated hydrographic sections, and long fixed stations spanning several semi-diurnal tidal cycles with microstructure measurements in the hot spots of internal tide generation and dissipation as well as in propagation direction will provide further insight into the internal tide life cycle south of New Caledonia, in combination with the SWOT data. Our simulations will help link the full water column dynamics and the SSH measurements.

Finally, this study provided first hints on the internal tides dissipation spatial variability. Yet, the impact of tidally-driven mixing on temperature, other tracer fields, and biological variables in this area of high biodiversity remains to be quantified. It is expected that strong vertical velocities along bathymetric slopes, reefs, and seamounts may influence nutrients inputs into the euphotic layer, primary production, potentially up to high trophic levels and marine fauna (Derville et al., 2020). Such effort has been recently initialized in the framework of the ScInObs (Science, Innovation and Observatories of seamounts) project led by the French Research Institute for Exploitation of the Sea (IFREMER) and in collaboration with the Japan Agency for Marine-Earth Science and Technology (JAMSTEC) south of New Caledonia at the Stylaster seamount (Fig. 12). Overall, observing and understanding the local impact of internal tides on the ecosystem is of large socio-economic interest for the island's conservation management. We hope that our results will pave the way to a better understanding of the processes and ultimately help for marine conservation.

*Code availability.* The tidal analysis was performed using the COMODO-SIROCCO tools which are developed and maintained by the SIROCCO national service (CNRS/INSU). SIROCCO is funded by INSU and Observatoire Midi-Pyrénées/Université Paul Sabatier and receives project support from CNES, SHOM, IFREMER and ANR.

*Author contributions.* AB performed the analysis and drafted the manuscript under the supervision of LG and SC. LB and AA performed the numerical simulations. The tidal analysis was performed with help of MT and FL including fruitful discussions with CV. All co-authors reviewed the manuscript and contributed to the writing and final editing.

*Competing interests.* The authors declare that they have no conflict of interest.

*Acknowledgements.* This work was performed within the PhD program of AB funded by the Faculty of Science and Engineering, University of Toulouse III - Paul-Sabatier and granted by the doctoral school Geosciences, Astrophysics, Space and Environmental Sciences (SDU2E). LG and SC are funded by the Institut de Recherche pour le Développement (IRD); LB and AA were funded by OceanNext, Grenoble; MT was funded by the Centre National d'Études Spatiale (CNES) and FL was funded by the Centre National de la Recherche Scientifique (CNRS); CV was funded by the Institut français de recherche pour l'exploitation de la mer (IFREMER). This work is a contribution to the joint CNES-NASA project *SWOT in the Tropics* and is supported by the French TOSCA (la Terre, l'Océan, les Surfaces Continentales, l'Atmosphère) program and the French national program LEFE (Les Enveloppes Fluides et l'Environnement). Simulations presented in this study were performed at the Centre Informatique National de l'Enseignement Supérieur (CINES). We thank the MEOM/IGE (MultiscalE Ocean Modeling/Institut des Géosciences de l'Environnement) group to be part of their allocation of computational resources. This study has been partially supported through the grant EUR TESS N°ANR-18-EURE-0018 in the framework of the Programme des Investissements d'Avenir. This study has been conducted using E.U. Copernicus Marine Service Information CMEMS (https://doi.org/10.48670/moi-00148). Climatological hydrography data was obtained from CARS (http://www.marine.csiro.au/~dunn/cars2009/). FES2014 was produced by Noveltis, LEGOS, and CLS and distributed by Aviso+, with support from CNES (https://www.aviso.altimetry.fr/). We acknowledge the publicly available HRET products from Edward Zaron (https://ingria.ceoas.oregonstate.edu/~zarone/downloads.html). Figures were created using Python 3.9, Matplotlib 3.5.1, and colormaps provided by Thyng et al. (2016) and van der Velden (2020). We thank Mathilde Cancet for the preparation of the bathymetry dataset and Amélie Ferran for preliminary work on the modeling and analysis of internal tides around New Caledonia. Further, we appreciate the fruitful discussions with Jerome Chanut, Julien Le Sommer as well as Ritabrata Thakur and Brian Arbic with helpful comments on the modeling part. We also thank the SWOT Science Teams *High-resolution Ocean Modeling Group* (led by Brian Arbic, Florent Lyard, and Lionel Renault) and *Tides, Internal Tides, and Internal Gravity Waves* (led by Edward Zaron and Brian Arbic) providing a platform for scientific exchanges and discussion. Finally, we thank two anonymous reviewers for the insightful suggestions that improved the manuscript.

## 730  References

Alford, M. H.: Redistribution of energy available for ocean mixing by long-range propagation of internal waves, Nature, 423, 159–162, https://doi.org/10.1038/nature01628, 2003.

Alford, M. H., MacKinnon, J. A., Nash, J. D., Simmons, H., Pickering, A., Klymak, J. M., Pinkel, R., Sun, O., Rainville, L., Musgrave, R., et al.: Energy flux and dissipation in Luzon Strait: Two tales of two ridges, Journal of Physical Oceanography, 41, 2211–2222, https://doi.org/10.1175/JPO-D-11-073.1, 2011.

Alford, M. H., Simmons, H. L., Marques, O. B., and Girton, J. B.: Internal tide attenuation in the North Pacific, Geophysical Research Letters, 46, 8205–8213, https://doi.org/10.1029/2019GL082648, 2019.

Ansong, J. K., Arbic, B. K., Simmons, H. L., Alford, M. H., Buijsman, M. C., Timko, P. G., Richman, J. G., Shriver, J. F., and Wallcraft, A. J.: Geographical distribution of diurnal and semidiurnal parametric subharmonic instability in a global ocean circulation model, Journal of Physical Oceanography, 48, 1409–1431, https://doi.org/10.1175/JPO-D-17-0164.1, 2018.

Arbic, B. K., Alford, M. H., Ansong, J. K., Buijsman, M. C., Ciotti, R. B., Farrar, J. T., Hallberg, R. W., Henze, C. E., Hill, C. N., Luecke, C. A., et al.: Primer on global internal tide and internal gravity wave continuum modeling in HYCOM and MITgcm, New frontiers in operational oceanography, pp. 307–392, http://purl.flvc.org/fsu/fd/FSU_libsubv1_scholarship_submission_1536242074_55feafcc, 2018.

Baker, L. E. and Sutherland, B. R.: The evolution of superharmonics excited by internal tides in non-uniform stratification, Journal of Fluid Mechanics, 891, R1, https://doi.org/10.1017/jfm.2020.188, 2020.

Balidakis, K., Sulzbach, R., Shihora, L., Dahle, C., Dill, R., and Dobslaw, H.: Atmospheric contributions to global ocean tides for satellite gravimetry, Journal of Advances in Modeling Earth Systems, 14, e2022MS003 193, https://doi.org/10.1029/2022MS003193, 2022.

Ballarotta, M., Ubelmann, C., Pujol, M.-I., Taburet, G., Fournier, F., Legeais, J.-F., Faugère, Y., Delepoulle, A., Chelton, D., Dibarboure, G., et al.: On the resolutions of ocean altimetry maps, Ocean Science, 15, 1091–1109, https://doi.org/10.5194/os-15-1091-2019, 2019.

Balmforth, N., Ierley, G., and Young, W.: Tidal conversion by subcritical topography, Journal of Physical Oceanography, 32, 2900–2914, https://doi.org/10.1175/1520-0485(2002)032<2900:TCBST>2.0.CO;2, 2002.

Bell Jr, T.: Topographically generated internal waves in the open ocean, Journal of Geophysical Research, 80, 320–327, https://doi.org/10.1029/JC080i003p00320, 1975.

Buijsman, M. C., Klymak, J. M., Legg, S., Alford, M. H., Farmer, D., MacKinnon, J. A., Nash, J. D., Park, J.-H., Pickering, A., and Simmons, H.: Three-dimensional double-ridge internal tide resonance in Luzon Strait, Journal of Physical Oceanography, 44, 850–869, https://doi.org/10.1175/JPO-D-13-024.1, 2014.

Buijsman, M. C., Arbic, B. K., Richman, J. G., Shriver, J. F., Wallcraft, A. J., and Zamudio, L.: Semidiurnal internal tide incoherence in the equatorial p acific, Journal of Geophysical Research: Oceans, 122, 5286–5305, https://doi.org/10.1002/2016JC012590, 2017.

Buijsman, M. C., Stephenson, G. R., Ansong, J. K., Arbic, B. K., Green, J. M., Richman, J. G., Shriver, J. F., Vic, C., Wallcraft, A. J., and Zhao, Z.: On the interplay between horizontal resolution and wave drag and their effect on tidal baroclinic mode waves in realistic global ocean simulations, Ocean Modelling, 152, 101 656, https://doi.org/10.1016/j.ocemod.2020.101656, 2020.

Carrere, L., Arbic, B. K., Dushaw, B., Egbert, G., Erofeeva, S., Lyard, F., Ray, R. D., Ubelmann, C., Zaron, E., Zhao, Z., et al.: Accuracy assessment of global internal-tide models using satellite altimetry, Ocean Science, 17, 147–180, https://doi.org/10.5194/os-17-147-2021, 2021.

765  Carter, G. S., Merrifield, M., Becker, J. M., Katsumata, K., Gregg, M., Luther, D., Levine, M., Boyd, T. J., and Firing, Y.: Energetics of M 2 barotropic-to-baroclinic tidal conversion at the Hawaiian Islands, Journal of Physical Oceanography, 38, 2205–2223, https://doi.org/10.1175/2008JPO3860.1, 2008.

Chapman, S. and Lindzen, R. S.: Atmospheric tides: thermal and gravitational, vol. 15, Springer Science & Business Media, https://doi.org/10.1007/978-94-010-3399-2, 1969.

770  Couvelard, X.: Structure et dynamique des jets barotropes créés pas les îles du Pacifique Sud-Ouest., Ph.D. thesis, Université Paul Sabatier-Toulouse III, 2007.

Couvelard, X., Marchesiello, P., Gourdeau, L., and Lefèvre, J.: Barotropic zonal jets induced by islands in the southwest Pacific, Journal of Physical Oceanography, 38, 2185–2204, https://doi.org/10.1175/2008JPO3903.1, 2008.

Cravatte, S., Kestenare, E., Eldin, G., Ganachaud, A., Lefèvre, J., Marin, F., Menkes, C., and Aucan, J.: Regional circulation around New
775     Caledonia from two decades of observations, Journal of Marine Systems, 148, 249–271, https://doi.org/10.1016/j.jmarsys.2015.03.004, 2015.

de Lavergne, C., Falahat, S., Madec, G., Roquet, F., Nycander, J., and Vic, C.: Toward global maps of internal tide energy sinks, Ocean Modelling, 137, 52–75, https://doi.org/10.1016/j.ocemod.2019.03.010, 2019.

de Lavergne, C., Vic, C., Madec, G., Roquet, F., Waterhouse, A. F., Whalen, C., Cuypers, Y., Bouruet-Aubertot, P., Ferron, B., and Hi-
780     biya, T.: A parameterization of local and remote tidal mixing, Journal of Advances in Modeling Earth Systems, 12, e2020MS002 065, https://doi.org/10.1029/2020MS002065, 2020.

Debreu, L., Vouland, C., and Blayo, E.: AGRIF: Adaptive grid refinement in Fortran, Computers & Geosciences, 34, 8–13, https://doi.org/10.1016/j.cageo.2007.01.009, 2008.

Derville, S., Torres, L. G., Zerbini, A. N., Oremus, M., and Garrigue, C.: Horizontal and vertical movements of humpback whales inform
785     the use of critical pelagic habitats in the western South Pacific, Scientific Reports, 10, 4871, https://doi.org/10.1038/s41598-020-61771-z, 2020.

Dufau, C., Orsztynowicz, M., Dibarboure, G., Morrow, R., and Le Traon, P.-Y.: Mesoscale resolution capability of altimetry: Present and future, Journal of Geophysical Research: Oceans, 121, 4910–4927, https://doi.org/10.1002/2015JC010904, 2016.

Dunphy, M. and Lamb, K. G.: Focusing and vertical mode scattering of the first mode internal tide by mesoscale eddy interaction, Journal of
790     Geophysical Research: Oceans, 119, 523–536, https://doi.org/10.1002/2013JC009293, 2014.

Dunphy, M., Ponte, A. L., Klein, P., and Le Gentil, S.: Low-mode internal tide propagation in a turbulent eddy field, Journal of Physical Oceanography, 47, 649–665, https://doi.org/10.1175/JPO-D-16-0099.1, 2017.

Durand, F., Marin, F., Fuda, J.-L., and Terre, T.: The east caledonian current: a case example for the intercomparison between altika and in situ measurements in a boundary current, Marine Geodesy, 40, 1–22, https://doi.org/10.1080/01490419.2016.1258375, 2017.

795  Dushaw, B. D., Howe, B. M., Cornuelle, B. D., Worcester, P. F., and Luther, D. S.: Barotropic and baroclinic tides in the central North Pacific Ocean determined from long-range reciprocal acoustic transmissions, Journal of Physical Oceanography, 25, 631–647, https://doi.org/10.1175/1520-0485(1995)025<0631:BABTIT>2.0.CO;2, 1995.

d'Ovidio, F., Pascual, A., Wang, J., Doglioli, A. M., Jing, Z., Moreau, S., Grégori, G., Swart, S., Speich, S., Cyr, F., et al.: Frontiers in fine-scale in situ studies: Opportunities during the swot fast sampling phase, Frontiers in Marine Science, 6, 168,
800     https://doi.org/10.3389/fmars.2019.00168, 2019.

Falahat, S., Nycander, J., Roquet, F., and Zarroug, M.: Global calculation of tidal energy conversion into vertical normal modes, Journal of Physical Oceanography, 44, 3225–3244, https://doi.org/10.1175/JPO-D-14-0002.1, 2014.

Fu, L.-L. and Ferrari, R.: Observing oceanic submesoscale processes from space, Eos, Transactions American Geophysical Union, 89, 488–488, https://doi.org/10.1029/2008EO480003, 2008.

805 Fu, L.-L. and Ubelmann, C.: On the transition from profile altimeter to swath altimeter for observing global ocean surface topography, Journal of Atmospheric and Oceanic Technology, 31, 560–568, https://doi.org/10.1175/JTECH-D-13-00109.1, 2014.

Fu, L.-L., Alsdorf, D., Morrow, R., Rodriguez, E., and Mognard, N.: SWOT: the Surface Water and Ocean Topography Mission: wide-swath altimetric elevation on Earth, Tech. rep., Pasadena, CA: Jet Propulsion Laboratory, National Aeronautics and Space . . . , http://hdl.handle.net/2014/41996, 2012.

810 Ganachaud, A., Vega, A., Rodier, M., Dupouy, C., Maes, C., Marchesiello, P., Eldin, G., Ridgway, K., and Le Borgne, R.: Observed impact of upwelling events on water properties and biological activity off the southwest coast of New Caledonia, Marine Pollution Bulletin, 61, 449–464, https://doi.org/10.1016/j.marpolbul.2010.06.042, 2010.

Gardes, L., Tessier, E., Allain, V., Alloncle, N., Baudat-Franceschi, J., Butaud, J., Collot, J., Etaix-Bonnin, R., Hubert, A., Jourdan, H., et al.: Analyse stratégique de l'Espace maritime de la Nouvelle-Calédonie–vers une gestion intégrée, Nouméa: Agence des aires marines 815 protégées, https://doi.org/10.13140/RG.2.1.2888.0803, 2014.

Garrett, C. and Kunze, E.: Internal tide generation in the deep ocean, Annu. Rev. Fluid Mech., 39, 57–87, https://doi.org/10.1146/annurev.fluid.39.050905.110227, 2007.

Gaspar, P., Grégoris, Y., and Lefevre, J.-M.: A simple eddy kinetic energy model for simulations of the oceanic vertical mixing: Tests at station Papa and Long-Term Upper Ocean Study site, Journal of Geophysical Research: Oceans, 95, 16 179–16 193, 820 https://doi.org/10.1029/JC095iC09p16179, 1990.

GEBCO, B.: The GEBCO_2019 Grid–a Continuous Terrain Model of the Global Oceans and Land, BODC [data set], 2019.

Gerkema, T.: Internal and interfacial tides: beam scattering and local generation of solitary waves, Journal of Marine Research, 59, 227–255, https://doi.org/10.1357/002224001762882646, 2001.

Gill, A. E.: Atmosphere-ocean dynamics, vol. 30, Academic press, 1982.

825 Hendershott, M. C.: Long waves and ocean tides, Evolution of physical oceanography, 1981.

Hersbach, H., Bell, B., Berrisford, P., Hirahara, S., Horányi, A., Muñoz-Sabater, J., Nicolas, J., Peubey, C., Radu, R., Schepers, D., et al.: The ERA5 global reanalysis, Quarterly Journal of the Royal Meteorological Society, 146, 1999–2049, https://doi.org/10.1002/qj.3803, 2020.

Jeon, C.-H., Buijsman, M. C., Wallcraft, A. J., Shriver, J. F., Arbic, B. K., Richman, J. G., and Hogan, P. J.: Improving surface tidal accuracy through two-way nesting in a global ocean model, Ocean Modelling, 137, 98–113, https://doi.org/10.1016/j.ocemod.2019.03.007, 2019.

830 Kelly, S., Nash, J., and Kunze, E.: Internal-tide energy over topography, Journal of Geophysical Research: Oceans, 115, https://doi.org/10.1029/2009JC005618, 2010.

Kelly, S., Jones, N., Nash, J., and Waterhouse, A.: The geography of semidiurnal mode-1 internal-tide energy loss, Geophysical Research Letters, 40, 4689–4693, https://doi.org/10.1002/grl.50872, 2013.

Keppler, L., Cravatte, S., Chaigneau, A., Pegliasco, C., Gourdeau, L., and Singh, A.: Observed characteristics and vertical 835 structure of mesoscale eddies in the southwest tropical Pacific, Journal of Geophysical Research: Oceans, 123, 2731–2756, https://doi.org/10.1002/2017JC013712, 2018.

Kerry, C. G., Powell, B. S., and Carter, G. S.: Effects of remote generation sites on model estimates of M2 internal tides in the Philippine Sea, Journal of Physical Oceanography, 43, 187–204, https://doi.org/10.1175/JPO-D-12-081.1, 2013.

Kessler, W. S. and Cravatte, S.: Mean circulation of the Coral Sea, Journal of Geophysical Research: Oceans, 118, 6385–6410, 840 https://doi.org/10.1002/2013JC009117, 2013.

Kunze, E.: Internal-wave-driven mixing: Global geography and budgets, Journal of Physical Oceanography, 47, 1325–1345, https://doi.org/10.1175/JPO-D-16-0141.1, 2017a.

Kunze, E.: The internal-wave-driven meridional overturning circulation, Journal of Physical Oceanography, 47, 2673–2689, https://doi.org/10.1175/JPO-D-16-0141.1, 2017b.

845 Lahaye, N., Gula, J., and Roullet, G.: Sea surface signature of internal tides, Geophysical Research Letters, 46, 3880–3890, https://doi.org/10.1029/2018GL081848, 2019.

Lahaye, N., Gula, J., and Roullet, G.: Internal Tide Cycle and Topographic Scattering Over the North Mid-Atlantic Ridge, Journal of Geophysical Research: Oceans, 125, e2020JC016376, https://doi.org/10.1029/2020JC016376, 2020.

Lamb, K. G. and Dunphy, M.: Internal wave generation by tidal flow over a two-dimensional ridge: Energy flux asymmetries induced by a 850 steady surface trapped current, Journal of Fluid Mechanics, 836, 192–221, https://doi.org/10.1017/jfm.2017.800, 2018.

Laurent, L. C. S. and Nash, J. D.: An examination of the radiative and dissipative properties of deep ocean internal tides, Deep Sea Research Part II: Topical Studies in Oceanography, 51, 3029–3042, https://doi.org/10.1016/j.dsr2.2004.09.008, 2004.

Laurent, L. S., Stringer, S., Garrett, C., and Perrault-Joncas, D.: The generation of internal tides at abrupt topography, Deep Sea Research Part I: Oceanographic Research Papers, 50, 987–1003, https://doi.org/10.1016/S0967-0637(03)00096-7, 2003.

855 Le Traon, P.-Y., Klein, P., Hua, B. L., and Dibarboure, G.: Do altimeter wavenumber spectra agree with the interior or surface quasigeostrophic theory?, Journal of Physical Oceanography, 38, 1137–1142, https://doi.org/10.1175/2007JPO3806.1, 2008.

Legg, S. and Huijts, K. M.: Preliminary simulations of internal waves and mixing generated by finite amplitude tidal flow over isolated topography, Deep Sea Research Part II: Topical Studies in Oceanography, 53, 140–156, https://doi.org/10.1016/j.dsr2.2005.09.014, 2006.

Leichter, J. J., Stewart, H. L., and Miller, S. L.: Episodic nutrient transport to Florida coral reefs, Limnology and Oceanography, 48, 1394–860 1407, https://doi.org/10.4319/lo.2003.48.4.1394, 2003.

Lyard, F. H., Allain, D. J., Cancet, M., Carrère, L., and Picot, N.: FES2014 global ocean tide atlas: design and performance, Ocean Science, 17, 615–649, https://doi.org/10.5194/os-17-615-2021, 2021.

MacKinnon, J. A., Zhao, Z., Whalen, C. B., Waterhouse, A. F., Trossman, D. S., Sun, O. M., Laurent, L. C. S., Simmons, H. L., Polzin, K., Pinkel, R., et al.: Climate process team on internal wave–driven ocean mixing, Bulletin of the American Meteorological Society, 98, 865 2429–2454, https://doi.org/10.1175/BAMS-D-16-0030.1, 2017.

Madec, G. and Team, N. S.: NEMO ocean engine, no. 27 in Scientific Notes of Climate Modelling Center, Zenodo, https://doi.org/10.5281/zenodo.1464816, backup Publisher: Institut Pierre-Simon Laplace (IPSL) ISSN: 1288-1619.

Mazloff, M. R., Cornuelle, B., Gille, S. T., and Wang, J.: The Importance of Remote Forcing for Regional Modeling of Internal Waves, Journal of Geophysical Research: Oceans, 125, https://doi.org/10.1029/2019JC015623, 2020.

870 McDougall, T. J. and Barker, P. M.: Getting started with TEOS-10 and the Gibbs Seawater (GSW) oceanographic toolbox, Scor/Iapso WG, 127, 1–28, 2011.

Melet, A., Hallberg, R., Legg, S., and Polzin, K.: Sensitivity of the ocean state to the vertical distribution of internal-tide-driven mixing, Journal of Physical Oceanography, 43, 602–615, https://doi.org/10.1175/JPO-D-12-055.1, 2013.

Menkès, C. E., Allain, V., Rodier, M., Gallois, F., Lebourges-Dhaussy, A., Hunt, B. P., Smeti, H., Pagano, M., Josse, E., Daroux, A., et al.: 875 Seasonal oceanography from physics to micronekton in the south-west Pacific, Deep Sea Research Part II: Topical Studies in Oceanography, 113, 125–144, https://doi.org/10.1016/j.dsr2.2014.10.026, 2015.

Merrifield, M. A. and Holloway, P. E.: Model estimates of M2 internal tide energetics at the Hawaiian Ridge, Journal of Geophysical Research: Oceans, 107, 5–1, https://doi.org/10.1029/2001JC000996, 2002.

Morrow, R., Fu, L.-L., Ardhuin, F., Benkiran, M., Chapron, B., Cosme, E., d'Ovidio, F., Farrar, J. T., Gille, S. T., Lapeyre, G., et al.: Global observations of fine-scale ocean surface topography with the Surface Water and Ocean Topography (SWOT) mission, Frontiers in Marine Science, 6, 232, https://doi.org/10.3389/fmars.2019.00232, 2019.

Munk, W. and Wunsch, C.: Abyssal recipes II: Energetics of tidal and wind mixing, Deep Sea Research Part I: Oceanographic Research Papers, 45, 1977–2010, https://doi.org/10.1016/S0967-0637(98)00070-3, 1998.

Nelson, A., Arbic, B., Menemenlis, D., Peltier, W., Alford, M., Grisouard, N., and Klymak, J.: Improved internal wave spectral continuum in a regional ocean model, Journal of Geophysical Research: Oceans, 125, e2019JC015 974, https://doi.org/10.1029/2019JC015974, 2020.

Niwa, Y. and Hibiya, T.: Numerical study of the spatial distribution of the M2 internal tide in the Pacific Ocean, Journal of Geophysical Research: Oceans, 106, 22 441–22 449, https://doi.org/10.1029/2000JC000770, 2001.

Niwa, Y. and Hibiya, T.: Three-dimensional numerical simulation of M2 internal tides in the East China Sea, Journal of Geophysical Research: Oceans, 109, https://doi.org/10.1029/2003JC001923, 2004.

Nugroho, D.: The tides in a general circulation model in the indonesian sras, Ph.D. thesis, Université Paul Sabatier-Toulouse III, 2017.

Nycander, J.: Generation of internal waves in the deep ocean by tides, Journal of Geophysical Research: Oceans, 110, https://doi.org/10.1029/2004JC002487, 2005.

Olbers, D., Pollmann, F., and Eden, C.: On PSI interactions in internal gravity wave fields and the decay of baroclinic tides, Journal of Physical Oceanography, 50, 751–771, https://doi.org/10.1175/JPO-D-19-0224.1, 2020.

Payri, C.-E. and de Forges, B. R.: Compendium of marine species from New Caledonia, IRD (Institut de recherche pour le développement), 2006.

Payri, C. E., Allain, V., Aucan, J., David, C., David, V., Dutheil, C., Loubersac, L., Menkes, C., Pelletier, B., Pestana, G., et al.: New caledonia, in: World Seas: An Environmental Evaluation, pp. 593–618, Elsevier, https://doi.org/10.1016/B978-0-08-100853-9.00035-X, 2019.

Pelletier, B.: Geology of the New Caledonia region and its implications for the study of the New Caledonian biodiversity, Compendium of marines species from New Caledonia, Dossiers Scientifiques et Techniques, II7, pp. 19–32, 2007.

Ponte, A. L., Klein, P., Dunphy, M., and Le Gentil, S.: Low-mode internal tides and balanced dynamics disentanglement in altimetric observations: Synergy with surface density observations, Journal of Geophysical Research: Oceans, 122, 2143–2155, https://doi.org/10.1002/2016JC012214, 2017.

Qiu, B. and Chen, S.: Seasonal modulations in the eddy field of the South Pacific Ocean, Journal of Physical Oceanography, 34, 1515–1527, https://doi.org/10.1175/1520-0485(2004)034<1515:SMITEF>2.0.CO;2, 2004.

Qiu, B., Scott, R. B., and Chen, S.: Length scales of eddy generation and nonlinear evolution of the seasonally modulated South Pacific Subtropical Countercurrent, Journal of Physical Oceanography, 38, 1515–1528, https://doi.org/10.1175/2007JPO3856.1, 2008.

Qiu, B., Chen, S., and Kessler, W. S.: Source of the 70-day mesoscale eddy variability in the Coral Sea and the North Fiji Basin, Journal of Physical Oceanography, 39, 404–420, https://doi.org/10.1175/2008JPO3988.1, 2009.

Qiu, B., Chen, S., Klein, P., Wang, J., Torres, H., Fu, L.-L., and Menemenlis, D.: Seasonality in transition scale from balanced to unbalanced motions in the world ocean, Journal of Physical Oceanography, 48, 591–605, https://doi.org/10.1175/JPO-D-17-0169.1, 2018.

Qu, T. and Lindstrom, E. J.: A climatological interpretation of the circulation in the western South Pacific, Journal of Physical Oceanography, 32, 2492–2508, https://doi.org/10.1175/1520-0485(2002)032<2492:ACIOTC>2.0.CO;2, 2002.

Rainville, L. and Pinkel, R.: Propagation of low-mode internal waves through the ocean, Journal of Physical Oceanography, 36, 1220–1236, https://doi.org/10.1175/JPO2889.1, 2006.

Ray, R. D. and Zaron, E. D.: M2 internal tides and their observed wavenumber spectra from satellite altimetry, Journal of Physical Oceanography, 46, 3–22, https://doi.org/10.1175/JPO-D-15-0065.1, 2016.

Renault, L., Molemaker, M. J., McWilliams, J. C., Shchepetkin, A. F., Lemarié, F., Chelton, D., Illig, S., and Hall, A.: Modulation of wind work by oceanic current interaction with the atmosphere, Journal of Physical Oceanography, 46, 1685–1704, https://doi.org/10.1175/JPO-D-15-0232.1, 2016.

Ridgway, K. and Dunn, J.: Mesoscale structure of the mean East Australian Current System and its relationship with topography, Progress in oceanography, 56, 189–222, https://doi.org/10.1016/S0079-6611(03)00004-1, 2003.

Ridgway, K., Dunn, J., and Wilkin, J.: Ocean interpolation by four-dimensional weighted least squares—Application to the waters around Australasia, Journal of atmospheric and oceanic technology, 19, 1357–1375, https://doi.org/10.1175/1520-0426(2002)019<1357:OIBFDW>2.0.CO;2, 2002.

Roger, J., Pelletier, B., Duphil, M., Lefèvre, J., Aucan, J., Lebellegard, P., Thomas, B., Bachelier, C., and Varillon, D.: The Mw 7.5 Tadine (Maré, Loyalty Is.) earthquake and related tsunami of December 5, 2018: implications for tsunami hazard assessment in New Caledonia., Natural Hazards and Earth System Sciences, Discussions, https://doi. org/10.5194/nhess-2021-58, https://doi.org/10.5194/nhess-2021-58, 2021.

Samadi, S., Bottan, L., Macpherson, E., De Forges, B. R., and Boisselier, M.-C.: Seamount endemism questioned by the geographic distribution and population genetic structure of marine invertebrates, Marine Biology, 149, 1463–1475, https://doi.org/10.1007/s00227-006-0306-4, 2006.

Savage, A. C., Arbic, B. K., Alford, M. H., Ansong, J. K., Farrar, J. T., Menemenlis, D., O'Rourke, A. K., Richman, J. G., Shriver, J. F., Voet, G., et al.: Spectral decomposition of internal gravity wave sea surface height in global models, Journal of Geophysical Research: Oceans, 122, 7803–7821, https://doi.org/10.1002/2017JC013009, 2017.

Sérazin, G., Marin, F., Gourdeau, L., Cravatte, S., Morrow, R., and Dabat, M.-L.: Scale-dependent analysis of in situ observations in the mesoscale to submesoscale range around New Caledonia, Ocean Science, 16, 907–925, https://doi.org/10.5194/os-16-907-2020, 2020.

Shakespeare, C. J. and Hogg, A. M.: On the momentum flux of internal tides, Journal of Physical Oceanography, 49, 993–1013, https://doi.org/10.1175/JPO-D-18-0165.1, 2019.

Simmons, H. L., Hallberg, R. W., and Arbic, B. K.: Internal wave generation in a global baroclinic tide model, Deep Sea Research Part II: Topical Studies in Oceanography, 51, 3043–3068, https://doi.org/10.1016/j.dsr2.2004.09.015, 2004.

Siyanbola, O. Q., Buijsman, M. C., Delpech, A., Renault, L., Barkan, R., Shriver, J. F., Arbic, B. K., and McWilliams, J. C.: Remote internal wave forcing of regional ocean simulations near the US West Coast, Ocean Modelling, 181, 102 154, https://doi.org/10.1016/j.ocemod.2022.102154, 2023.

Smith, S. G. L. and Young, W.: Conversion of the barotropic tide, Journal of Physical Oceanography, 32, 1554–1566, https://doi.org/10.1175/1520-0485(2002)032<1554:COTBT>2.0.CO;2, 2002.

St. Laurent, L. and Garrett, C.: The role of internal tides in mixing the deep ocean, Journal of Physical Oceanography, 32, 2882–2899, https://doi.org/10.1175/1520-0485(2002)032<2882:TROITI>2.0.CO;2, 2002.

St. Laurent, L., Simmons, H., and Jayne, S.: Estimating tidally driven mixing in the deep ocean, Geophysical research letters, 29, 21–1, https://doi.org/10.1029/2002GL015633, 2002.

Sutherland, B. R. and Dhaliwal, M. S.: The nonlinear evolution of internal tides. Part 1: the superharmonic cascade, Journal of Fluid Mechanics, 948, A21, https://doi.org/10.1017/jfm.2022.689, 2022.

Tchilibou, M., Gourdeau, L., Lyard, F., Morrow, R., Koch Larrouy, A., Allain, D., and Djath, B.: Internal tides in the Solomon Sea in contrasted ENSO conditions, Ocean Science, 16, 615–635, https://doi.org/10.5194/os-16-615-2020, 2020.

Tchilibou, M., Koch-Larrouy, A., Barbot, S., Lyard, F., Morel, Y., Jouanno, J., and Morrow, R.: Internal tides off the Amazon shelf during two contrasted seasons: interactions with background circulation and SSH imprints, Ocean Science, 18, 1591–1618, https://doi.org/10.5194/os-18-1591-2022, 2022.

Thakur, R., Arbic, B. K., Menemenlis, D., Momeni, K., Pan, Y., Peltier, W. R., Skitka, J., Alford, M. H., and Ma, Y.: Impact of vertical mixing parameterizations on internal gravity wave spectra in regional ocean models, Geophysical Research Letters, 49, e2022GL099 614, https://doi.org/10.1029/2022GL099614, 2022.

Thyng, K. M., Greene, C. A., Hetland, R. D., Zimmerle, H. M., and DiMarco, S. F.: True colors of oceanography: Guidelines for effective and accurate colormap selection, Oceanography, 29, 9–13, https://doi.org/10.5670/oceanog.2016.66, 2016.

Ubelmann, C., Carrere, L., Durand, C., Dibarboure, G., Faugère, Y., Ballarotta, M., Briol, F., and Lyard, F.: Simultaneous estimation of ocean mesoscale and coherent internal tide sea surface height signatures from the global altimetry record, Ocean Science, 18, 469–481, https://doi.org/10.5194/os-18-469-2022, 2022.

van der Velden, E.: CMasher: Scientific colormaps for making accessible, informative and 'cmashing' plots, The Journal of Open Source Software, 5, 2004, https://doi.org/10.21105/joss.02004, 2020.

Vergara, O., Morrow, R., Pujol, M.-I., Dibarboure, G., and Ubelmann, C.: Global submesoscale diagnosis using alongtrack satellite altimetry, EGUsphere, pp. 1–39, https://doi.org/10.5194/egusphere-2022-1073, 2022.

Vic, C., Garabato, A. C. N., Green, J. M., Spingys, C., Forryan, A., Zhao, Z., and Sharples, J.: The lifecycle of semidiurnal internal tides over the northern Mid-Atlantic Ridge, Journal of Physical Oceanography, 48, 61–80, https://doi.org/10.1175/JPO-D-17-0121.1, 2018.

Vic, C., Naveira Garabato, A. C., Green, J. M., Waterhouse, A. F., Zhao, Z., Melet, A., de Lavergne, C., Buijsman, M. C., and Stephenson, G. R.: Deep-ocean mixing driven by small-scale internal tides, Nature communications, 10, 2099, https://doi.org/10.1038/s41467-019-10149-5, 2019.

Waterhouse, A. F., MacKinnon, J. A., Nash, J. D., Alford, M. H., Kunze, E., Simmons, H. L., Polzin, K. L., Laurent, L. C. S., Sun, O. M., Pinkel, R., et al.: Global patterns of diapycnal mixing from measurements of the turbulent dissipation rate, Journal of Physical Oceanography, 44, 1854–1872, https://doi.org/10.1175/JPO-D-13-0104.1, 2014.

Wolanski, E. and Pickard, G.: Long-term observations of currents on the central Great Barrier Reef continental shelf, Coral Reefs, 4, 47–57, 1985.

Wyatt, A. S., Leichter, J. J., Toth, L. T., Miyajima, T., Aronson, R. B., and Nagata, T.: Heat accumulation on coral reefs mitigated by internal waves, Nature Geoscience, 13, 28–34, https://doi.org/10.1038/s41561-019-0486-4, 2020.

Wyatt, A. S., Leichter, J. J., Washburn, L., Kui, L., Edmunds, P. J., and Burgess, S. C.: Hidden heatwaves and severe coral bleaching linked to mesoscale eddies and thermocline dynamics, Nature Communications, 14, 25, https://doi.org/10.1038/s41467-022-35550-5, 2023.

Zaron, E. D.: Baroclinic tidal sea level from exact-repeat mission altimetry, Journal of Physical Oceanography, 49, 193–210, https://doi.org/10.1175/JPO-D-18-0127.1, 2019.

Zaron, E. D. and Egbert, G. D.: Estimating open-ocean barotropic tidal dissipation: The Hawaiian Ridge, Journal of Physical Oceanography, 36, 1019–1035, https://doi.org/10.1175/JPO2878.1, 2006.

Zhao, Z., Alford, M. H., MacKinnon, J. A., and Pinkel, R.: Long-range propagation of the semidiurnal internal tide from the Hawaiian Ridge, Journal of Physical Oceanography, 40, 713–736, https://doi.org/10.1175/2009JPO4207.1, 2010.

Zhao, Z., Alford, M. H., Girton, J. B., Rainville, L., and Simmons, H. L.: Global observations of open-ocean mode-1 M 2 internal tides, Journal of Physical Oceanography, 46, 1657–1684, https://doi.org/10.1175/JPO-D-15-0105.1, 2016.

Zilberman, N., Becker, J., Merrifield, M., and Carter, G.: Model estimates of M2 internal tide generation over Mid-Atlantic Ridge topography, Journal of Physical Oceanography, 39, 2635–2651, https://doi.org/10.1175/2008JPO4136.1, 2009.

995 Zilberman, N., Merrifield, M., Carter, G., Luther, D., Levine, M., and Boyd, T. J.: Incoherent nature of M 2 internal tides at the Hawaiian Ridge, Journal of physical oceanography, 41, 2021–2036, https://doi.org/10.1175/JPO-D-10-05009.1, 2011.

**Table A1.** Regional M2 barotropic energy flux divergence $\nabla F_{bt}$, barotropic energy dissipation $D_{bt}$, barotropic-to-baroclinic conversion $C$, baroclinic energy flux divergence $\nabla F_{bc}$, and baroclinic dissipation $D_{bc}$ integrated over the *North* (1), *South* (2), *Norfolk Ridge* (3), *Loyalty Ridge* (4) domains. The vertical structure for modes 1-4 are given for $C$ and $\nabla F_{bc}$.

|  |  | North | South | Norfolk Ridge | Loyalty Ridge |
|---|---|---|---|---|---|
| $\nabla F_{bt}$ |  | -3.83 | -6.16 | -3.51 | -1.28 |
| $D_{bt}$ |  | 1.66 | 2.24 | 1.47 | 0.31 |
| $C$ | total | 2.17 | 3.92 | 2.04 | 0.97 |
|  | mode 1 | 1.63 | 3.31 | 1.56 | 0.42 |
|  | mode 2 | 0.27 | 0.33 | 0.25 | 0.31 |
|  | mode 3 | 0.13 | 0.14 | 0.08 | 0.10 |
|  | mode 4 | 0.06 | 0.08 | 0.05 | 0.05 |
| $\nabla F_{bc}$ | total | 1.47 | 1.83 | 0.96 | 0.53 |
|  | mode 1 | 1.30 | 1.58 | 0.86 | 0.38 |
|  | mode 2 | 0.16 | 0.20 | 0.09 | 0.12 |
|  | mode 3 | < -0.01 | 0.02 | < 0.01 | 0.01 |
|  | mode 4 | 0.01 | 0.01 | < 0.01 | 0.01 |
| $D_{bc}$ | total | 0.70 | 2.09 | 1.07 | 0.44 |

All units are given in [GW].